PAPER

Check for updates

Tuning the opto-electronic properties of BaTiO₃ by S substitution towards energy harvesting applications: a DFT insight using the VASP code

U. Ahmed,[ab] M. M. Hossian,[a] M. M. Uddin,[a] N. Jahan[a] and M. A. Ali[*a]

This study explored the structural, electrical, optical, mechanical, and thermal properties of sulfur-substituted barium titanate perovskites ($BaTiO_{3-x}S_x$) using first-principles density functional theory (DFT) calculations, implemented in the Vienna *Ab initio* Simulation Package (VASP). Sulfur (S) substitution at oxygen (O) sites led to the formation of $BaTiO_2S$, $BaTiOS_2$, and $BaTiS_3$. The formation energy, tolerance factors, and AIMD simulation ensured the structural stability of these phases. The band structure calculation revealed a reduction of band gap from 3.069 eV ($BaTiO_3$) to 1.55, 1.02, and 0.35 eV for $BaTiO_2S$, $BaTiOS_2$, and $BaTiS_3$, respectively. The optical properties calculations revealed that the S substitution enhances the absorption coefficient, improving the optical properties in the visible range. The reduction of the band gap, which enhances the optical properties, has been explained in terms of the partial density of states (PDOS). The mechanical stability of the $BaTiO_{3-x}S_x$ compounds was confirmed by calculating the elastic constants. The changes in chemical bonding due to S substitution result in a variation in the elastic moduli. The effect of S substitution on the thermal properties was also studied, and a significant decrease in lattice thermal conductivity was explained in terms of phonon scattering. The results obtained for $BaTiO_2S$ and $BaTiOS_2$ ordered cells were also cross-checked by performing calculations in supercell structures. The reduced band gap and high absorption coefficient of $BaTiO_2S$ and $BaTiOS_2$ suggest a possible use in solar energy harvesting, whereas $BaTiS_3$ could be a potential thermoelectric material (with low lattice thermal conductivity).

1. Introduction

The rise in energy consumption and the growing concern over climate change have motivated a shift from coal, oil, and gas. Such a shift, imperative due to the environmental impacts brought about by the extraction and combustion of fossil fuels, is, therefore, of utmost importance.[1,2] Greenhouse gases from fossil fuel combustion have given rise to global warming and subsequent climate change.[3] Addressing these issues requires looking into alternative energy sources while making sure to remain environmentally friendly.[4] Solar energy is therefore the most promising of the renewable energy options due to its abundance and wide availability.[5] Solar energy captured by photovoltaic technology is very popular nowadays. The PV market is currently dominated by crystalline silicon solar cells because of their high durability and efficiency. However, the

high cost of producing high-purity silicon and the intricate manufacturing processes pose significant challenges.[6] A viable substitute for silicon solar cells is perovskite solar cells.[7] Perovskites are substances that resemble the naturally occurring mineral perovskite in terms of their crystal structure. Their general formula is ABX_3, in which X is an anion and A and B are cations.[8,9] Perovskites have garnered considerable attention in solar energy conversion, owing to their exceptional optoelectronic properties and potential for high power conversion efficiencies.[10] Perovskites, in particular, can perform well despite flaws and defects. The power conversion efficiency of perovskite solar cells has risen recently and is now on par with silicon solar cells.[11] Perovskite oxides and halide–fluoride systems have recently been revitalized as viable thermoelectric materials due to advances in quantum and solid-state physics. Perovskites with semiconductor-like behavior have a good figure of merit, making them suitable for application in energy conversion and thermoelectric devices.[12,13] However, environmental factors like light, humidity, and high temperatures can affect their performance and speed up the degradation processes; their long-term stability is a significant obstacle to their widespread commercialization.[14,15]

a Advanced Computational Materials Research Laboratory (ACMRL), Department of Physics, Chittagong University of Engineering and Technology (CUET), Chattogram-4349, Bangladesh

b Department of Materials Science and Engineering, Rajshahi University of Engineering and Technology, Bangladesh

$BaTiO_3$ is one of the classical ferroelectric perovskite materials, and it possesses a unique group of properties.[16] Due to its large dielectric constant, $BaTiO_3$ finds application in capacitor devices, and due to its piezoelectricity, it is applied in sensors and actuators.[17] It has a high Curie temperature, the temperature at which the material starts losing its ferroelectric properties and turning into a paraelectric material. $BaTiO_3$ undergoes a series of phase transitions depending on temperature that influence its properties. When cooled, it passes through tetragonal, orthorhombic, and rhombohedral ferroelectric phases with spontaneous polarization in various crystallographic directions.[18] Mishra et al.[19] synthesized the cubic phase from the tetragonal phase and studied the bandgap of $BaTiO_3$. For example, the band gap is 3.18 eV for the tetragonal phase and 3.12 eV for the cubic phase. The band gap of $BaTiO_3$ is around 3.2 eV,[20] and it lies in the ultraviolet region of the electromagnetic spectrum. $BaTiO_3$ is transparent in the visible spectrum, but it strongly absorbs UV light due to its band gap.[21] The refractive index and absorption coefficient of the compound have been determined by optical transmission measurements.[22]

The electronic structure and optical properties of $BaTiO_3$ make it suitable for application in several sectors. However, the large band gap (3.12 eV) limits its applications in energy harvesting technology, especially in photovoltaic solar cells.[23] Doping in materials has been a popular approach to reducing the bandgap. Gillani et al.[24] claim that Mg doping in $SrZrO_3$ makes it a strong candidate for optoelectronic applications by altering the electronic structure, imposing a direct bandgap at the Γ-point, and strengthening the Mg–O interactions that significantly impact their optical properties. Fe doping is especially promising for lead-free $CsSnCl_3$, according to Kholil et al.[25] Fe doping in $CsSnCl_3$ and $CsPbCl_3$ narrows the bandgap and adds donor states, enhancing absorption, conductivity, and optoelectronic performance. Adhikari et al.[26] investigated the effect of Mn^{2+} doping in $CsPbCl_3$ perovskite nanocrystals, which is regulated by alkylamine hydrochloride (RNH_3Cl), which functions as a chlorinating and growth-promoting agent to facilitate dopant incorporation, size control, and emission tuning. Tanwar et al.[27] synthesized Eu-doped $BaTiO_3$ using a solid-state method, which was demonstrated to have low overpotential, high stability, and increased electrocatalytic activity in the oxygen evolution reaction, offering a less expensive substitute for catalysts based on noble metals. Lou et al.[28] found that Li^+ doping in $BaTiO_3$ improves electric polarization and the internal electric field, optimizing electron transport properties and increasing the efficiency of perovskite solar cells by up to 14.3%. Yao et al.[29] reported that the effects of internal stress and grain size refinement, through Nd^{3+} doping of $BaTiO_3$, result in a tetragonal-to-cubic phase transition, modification of the Ti valence state, and an increase in permittivity, while exhibiting typical ferroelectric behavior.

Chalcogen anions such as sulfur (S) significantly contribute to bandgap reduction[30]. Li et al.[31] observed that sulfur anion doping in nanocubic $NaTaO_3$ results in a modulation of the band structure and lattice distortion, which greatly enhances visible light photocatalytic activity and charge carrier mobility, making it a viable option for solar oxidative pollution degradation. Jia et al.[32] demonstrate, using DFT, that sulfur doping in $LaBO_3$ (B = Fe, Co, Ni) perovskites promotes the formation of oxygen vacancies by lowering the lattice relaxation energy, thereby improving electrical conductivity and providing a general technique to enhance the functionalities of perovskites. Sulfur-doped oxide perovskites, such as $LaCoO_3$, show great potential for energy conversion and storage using Zn–air batteries because they exhibit improved conductivity and spin-state transitions that increase oxygen electrocatalysis, according to Ran et al.[33] Ech-Chargy et al.[34] found that when sulfur is added to $KTaO_3$ in amounts up to 12.5%, it lowers the bandgap from 3.86 eV to 1.24 eV and causes a direct bandgap transition. Hasina et al.[35,36] also investigated S-substituted $KTaO_3$ and $RbTaO_3$, which form $KTaO_2S$ and $RbTaO_2S$, respectively, and are suitable for solar energy conversion and optoelectronic applications due to their reduced band gaps. This higher sulfur content not only enhances the material's ability to absorb visible light but also alters the electronic structure, making it better suited for photocatalytic hydrogen production. Ahmed et al.[37] studied the effect of sulfur doping in $CsTaO_3$, which narrows the bandgap during phase changes, thereby improving the sample's absorption in the visible region and making it an efficient solar absorber with dynamic stability. Bennett et al.[38] employed first-principles simulations to study the effect of S substitution in $BaZrO_3$, which results in a lower band gap of $BaZrS_3$, and exhibits unique dielectric behavior due to variations in atomic mass, size, and covalency. Zhang et al.[39] demonstrated that only S, among all the anion dopants in $SrTiO_3$, effectively narrows the band gap by strongly mixing the S 3p and O 2p states, thereby improving the absorption of visible light.

Prior studies indicate that S incorporation in the perovskite structure significantly reduces the bandgap. However, what causes the bandgap to decrease when S is substituted? Sulfur substitution at oxygen sites is considered an attractive pathway due to this ion's initially favorable radius and chemical compatibility. The larger radius of the S^{2-} ion compared to O^{2-} forces lattice distortions, while its lower electronegativity enhances Ti–S covalent interactions and orbital hybridization, effectively narrowing the band gap and concomitantly increasing optical absorption in the visible range. The S-3p orbitals' energetic proximity to the upper valence band compared to the O-2p orbitals is one explanation. When S and O are exchanged, these S-3p orbitals can mix to form mid-gap states just above the valence band. The presence of a characteristic spectral signal near the absorption edge—often referred to as the "tail"—that extends into the visible spectrum has demonstrated the availability of these states. According to this behavior, S doping into O causes an enlarged valence band, which lowers the bandgap and improves the material's receptivity to visible light.[40] Thus, an expectation has grown among us that the S doping in $BaTiO_3$ could lower the band gap and make it suitable for use in solar cells as an absorbing layer. Furthermore, the more massive sulfur atom enhances phonon

scattering, which in turn reduces lattice thermal conductivity and is good for thermoelectric performance. All these factors make sulfur substitution a promising approach to engineer the optoelectronic and thermal properties of $BaTiO_{3-x}S_x$-based perovskites for energy applications. These are the prime motivations for this study.

Using DOS analysis, charge density mapping, and electronic band structure predictions, a thorough examination was conducted to determine the causes underlying this bandgap narrowing. The primary objective is to replace O with S to bring the bandgap of $BaTiO_3$ into the visible range. Achieving a high conversion efficiency in solar energy applications requires a bandgap close to the Shockley–Queisser limit[41]. Additionally, in semiconducting materials, bandgap narrowing enhances electrical conductivity, which is crucial for developing multifunctional materials with low energy costs.

In light of these factors, we investigate anion doping as a means of adjusting the electronic properties of the oxide perovskite $BaTiO_3$. To achieve this, a DFT-based simulation was performed to understand the impact of substituting S anions for O anions in $BaTiO_3$. The results show that adding S significantly reduces the bandgap, thereby improving optical absorption and ensuring higher mechanical and thermal stability, suitable for solar energy applications. These S-doped perovskites have an advantage in applications where thermal insulation is required to reduce lattice thermal conductivity.

Thus, in this paper, we examine the physical properties of the $BaTiO_{3-x}S_x$ series, including structural, electronic, optical, mechanical, and thermal properties, to explore their potential uses in various technologies. The electronic structure calculations indicate that these materials are suitable for use in solar cell technologies. The optical parameters, such as dielectric functions, absorption coefficient, and reflectivity, are considered in relation to solar applications. Mechanical strength and stability are evaluated through elastic constants, while thermal conductivity is analyzed to assess their suitability for thermoelectric applications. It is noted that the opto-electronic properties have been calculated using the hybrid functional, and the properties for $BaTiO_2S$ and $BaTiO_2S$ have been counter-checked by both ordered cell structures and super-cell structures.

2. Computational methodology

The density functional theory (DFT) calculations for the investigation of $BaTiO_{3-x}S_x$ were performed using the Vienna *ab initio* Simulation Package (VASP) using the projector augmented wave (PAW) basis.[42] The Perdew–Burke–Ernzerhof (PBE) functional, in conjunction with the generalized gradient approximation (GGA), was used to address the exchange–correlation interactions in solving the Kohn–Sham equations iteratively towards the ground-state electronic structure.[43] For accurate electronic band structure analysis, the hybrid Heyd–Scuseria–Ernzerhof (HSE06) functional was employed.[44] Valence electron configurations included Ba ($5s^2\ 5p^6\ 6s^2$), Ti ($3p^6\ 3d^2\ 4s^2$), O ($2s^2\ 2p^4$), and S ($3s^2\ 3p^4$). The energy

convergence and ionic convergence criteria were set to 1×10^{-6} eV and -2×10^{-2} eV Å^{-1}, respectively, for structural optimization. A plane-wave kinetic energy cutoff of 600 eV was used, and the Brillouin zone was sampled using Monkhorst–Pack k-point meshes of $6 \times 6 \times 6$ for the cubic unit cells, with adjustments for tetragonal geometries (*e.g.*, $6 \times 6 \times 5$ and $5 \times 5 \times 6$). By updating the charge density and calculating an effective potential to solve for a new wave function, the SCF iteration is carried out until convergence is reached.[45] VASPKit was used for post-processing analysis of the calculations, including density of states (DOS), band structure, and optical and mechanical properties.[46] To calculate the thermal properties, the phono3py and phonopy packages were utilized, which leverage third-order force constants and the Boltzmann transport equation under the relaxation time approximation.[47] To perform *ab initio* molecular dynamics (AIMD), the Cambridge serial total energy package (CASTEP) code has been used.[48]

3. Results and discussion

3.1 Structural properties and stability

The pristine $BaTiO_3$ [Fig. 1(a)] crystallizes in the perovskite structure (ABX_3), with Ba occupying the A-site, Ti at the B-site, and O at the anion sites. The cubic phase ($Pm\bar{3}m$) is stable at high temperatures and the atoms are arranged as follows: O is located at the center of the face (0, 0.5, 0.5), Ba is at the corner position (0, 0, 0), and Ti is at the center of the unit cell at coordinates (0.5, 0.5, 0.5)[19,49,50]. Upon substituting O with S, the phase shifts from the cubic to tetragonal phase ($P4/mm$). The following are the atomic positions of $BaTiO_2S$ [Fig. 1(b)] and $BaTiOS_2$ [Fig. 1(c)], respectively: Ba (0, 0, 0), Ti (0.5, 0.5, 0.5), O (0.5, 0, 0.5), and S (0, 0.5, 0.5) and Ti (0, 0, 0), Ba (0.5, 0.5, 0.5), S (0.5, 0, 0.5), and O (0.5, 0.5, 0). When three S atoms are added to the parent molecule, $BaTiS_3$ [Fig. 1(d)] is created, having the space group and Wyckoff positions of $BaTiO_3$, but the lattice parameter was extended due to S's larger ionic radius. The GGA–PBE approximation was employed to optimize the lattice parameter and unit cell volume. With the increase of S content, the volume of the unit cell increases from 65.6 Å^3 to 113.2 Å^3. The optimized lattice parameters for the cubic and tetragonal phases are summarized in Table 1.

To confirm the stability of these materials, the tolerance (T_F) factor and octahedral factor (μ) established by Goldschmidt have been calculated. The equations are given below:

$$T_F = \frac{R_A + R_X}{(\sqrt{2}R_B + R_X)} \quad (1)$$

$$\mu = \frac{R_B}{2R_X} \quad (2)$$

Here, the nomenclature is as follows: R_A is the radius of Ba; R_B is the radius of B-site ions (Ti); and R_X is the radius of O or S. The ionic radii of Shannon are the source of these values.[51] The tolerance factor (T_F) decreases with increasing atomic size. This number typically falls between 0.81 and 1.10, indicating the likelihood of a stable perovskite structure.[52] Additionally, the
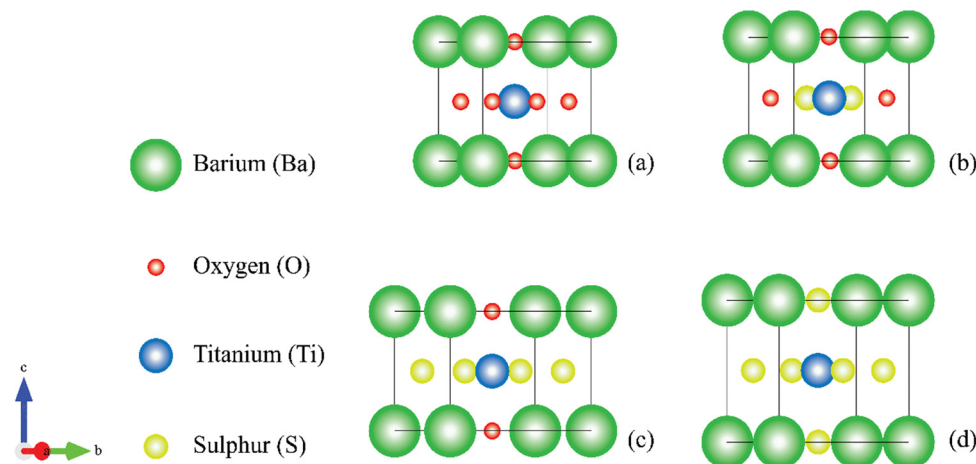
Fig. 1 The unit cell structure of (a) $BaTiO_3$, (b) $BaTiO_2S$, (c) $BaTiOS_2$ and (d) $BaTiS_3$.

cubic region, $0.38 < \mu < 0.90$, is where octahedral factors are advantageously positioned.[53] The computed values are shown in Table 1.

The chemical endurance of the semiconductor $BaTiO_{3-x}S_x$ perovskite has been further assessed by computing its formation energy (F.E.). An overview of the formula is provided below, as provided in ref. 54

$$E_{\text{Total}}^{BaTiO_{3-x}S_x} = \frac{E_{\text{for}}^{BaTiO_{3-x}S_x} - \left(AE_{\text{solid}}^{Ba} + BE_{\text{solid}}^{Ti} + CE_{\text{solid}}^{O} + DE_{\text{solid}}^{S}\right)}{A + B + C + D}$$

(3)

In the given equation, the variables A, B, C, and D correspond to the number of Ba, Ti, O, and S atoms in the unit cell. The terms $E_{\text{Total}}^{BaTiO_{3-x}S_x}$, E_{Solid}^{Ba}, E_{Solid}^{Ti}, E_{Solid}^{O}, and E_{Solid}^{S} represent the total energy of the $BaTiO_{3-x}S_x$ perovskite material and the corresponding solid-state energies of Ba, Ti, O, and S. The formation energy's negative sign validated their stability; Table 1 presents the calculated formation energy values. Since $BaTiO_3$ has already been experimentally synthesized, the calculated structural parameter, formation energy, and tolerance factor bolster the stability of the S-doped $BaTiO_{3-x}S_x$ compounds.

The total energy of $BaTiO_{3-x}S_x$ increases (becomes less negative) as sulfur concentration rises due to compositional and bonding factors. Replacing O with S weakens the Ti–X (X = O, S) bond and reduces the lattice cohesive energy because sulfur has a larger ionic radius and lower electronegativity than oxygen. The decrease in formation energy (less negative) with S substitution indicates that the oxides are more energetically

favorable and stable, while S-containing compositions are less stable compared to the oxide ones. However, S-containing compositions are still stable due to their negative formation energy.

Ab initio molecular dynamics (AIMD) calculations at 300 K for 10 ps were performed using an NVT ensemble to verify the thermal and structural stability of $BaTiO_3$, $BaTiO_2S$, $BaTiOS_2$, and $BaTiS_3$ under ambient conditions. Fig. 2 illustrates how the total energy of these four compounds changed over time during the simulation. The energy profile for $BaTiO_3$ is shown in Fig. 2(a), fluctuating between -3621.61 eV and -3616.49 eV, with an average of -3619.05 eV and a very low root-mean-square deviation of 0.0707%. Consistent with the well-established knowledge of $BaTiO_3$'s stability, this minimal change in average energy indicates its exceptional thermal stability. The results for $BaTiO_2S$ are displayed in Fig. 2(b), where the energy varies within a slightly narrower range (-3461.45 eV to -3456.85 eV) and exhibits a slightly smaller deviation of 0.0664%, suggesting that partial substitution of S does not impact the material's thermal stability or structural integrity. Conversely, Fig. 2(c) shows an additional minor decrease in energy fluctuation to 0.0627% with fully substituted $BaTiOS_2$, with extreme total energies of -3299.01 eV and -3303.15 eV. Such a smooth energy curve would indicate strong dynamic stability, achieved by increasing phonon scattering to prevent structural failure. Finally, panel (d) presents the AIMD results for $BaTiS_3$, which exhibits the lowest fluctuations (0.0547%) among the four systems. Despite complete chalcogenide substitution, the system's energy stabilizes at -3144.36 eV to -3140.92 eV, reflecting excellent thermal

Table 1 The optimized lattice parameters, a and c (both in Å), volume of the unit cell V (Å^3), and stability of perovskite $BaTiO_{3-x}S_x$ compounds

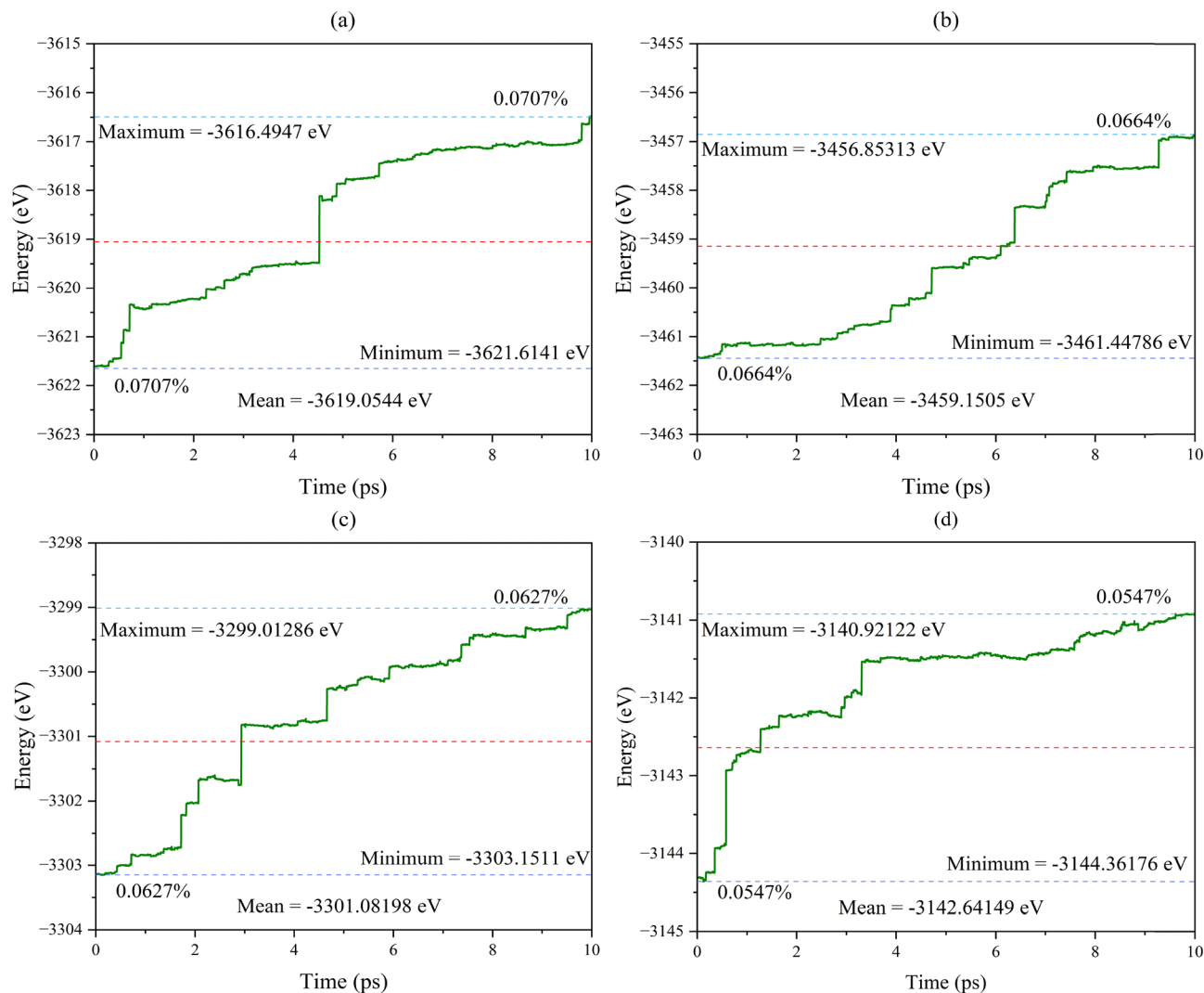| Compounds	a (Å)	c (Å)	V (Å^3)	Formation energy	T_F	μ	Ref.
$BaTiO_3$	4.032	—	65.6	-3.2288	1.061702	0.4235	This study
	4.01	—	64.37	-3.477	—	—	49
$BaTiO_2S$	4.136	4.842	82.8	-2.4916	1.037539	0.4678	This study
$BaTiOS_2$	5.018	3.887	97.9	-2.1509	1.016459	0.5122	This study
$BaTiS_3$	4.837	—	113.2	-1.6675	0.997909	0.5566	This study

Fig. 2 *Ab initio* molecular dynamics (AIMD) of (a) $BaTiO_3$, (b) $BaTiO_2S$, (c) $BaTiOS_2$, and (d) $BaTiS_3$ compounds.

resistance. Overall, there are no sudden energy jumps or discontinuities during the simulation, and all four compounds show very minimal energy drift ($<0.08\%$). This dynamic resilience arises because the negative formation energies and the prevailing Ti–anion covalency keep bonding cohesive as local geometries relax. In a nutshell, the anion substitution creates a more flexible environment (lower elastic moduli, higher polarizability), yet it cannot eliminate those bonding interactions that impart structural integrity under the influence of thermal agitation in ambient conditions.[55] These materials are among the most promising options for optoelectronic and thermoelectric applications, as they demonstrate both dynamic and thermal stability at room temperature.

3.2 Electronic properties

To comprehend the electronic properties of the $BaTaO_{3-x}S_x$ compounds, the electronic band structure (EBS), density of states (DOS), and charge density were computed to investigate the effects of sulfur (S) substitution. Electronic properties were calculated using both the GGA–PBE and HSE06 functionals. For semiconducting materials, local functionals such as GGA–PBE underestimate the bandgap.[56,57] To accurately predict the bandgap of semiconducting materials, a nonlocal functional (hybrid) HSE06, which incorporates 25% exact exchange and provides more accurate bandgap predictions, was utilized.[58–61] Gaussian smearing was used, and the smearing value was set to 0.1 eV. The estimated bandgap values are presented in Table 2. Fig. 3 presents the EBS of $BaTaO_{3-x}S_x$ compounds, where energy zero (E_f) was set to the Fermi level. The band structure of $BaTiO_3$ [Fig. 3(a)] exhibits an indirect bandgap, with the valence band maximum (VBM) located at the R-point and the conduction band minimum (CBM) at the G-point. This is consistent with previous theoretical and experimental studies.[23] The calculated bandgap of $BaTiO_3$ is 3.0691 eV, which agrees with known values for its cubic phase.[19] Upon substituting oxygen (O) atom(s) with sulfur (S) in $BaTiO_2S$ and $BaTiOS_2$ [Fig. 3(b) and (c)], the band structure shows significant modifications, and the band gaps are also reduced to 1.5501 eV and
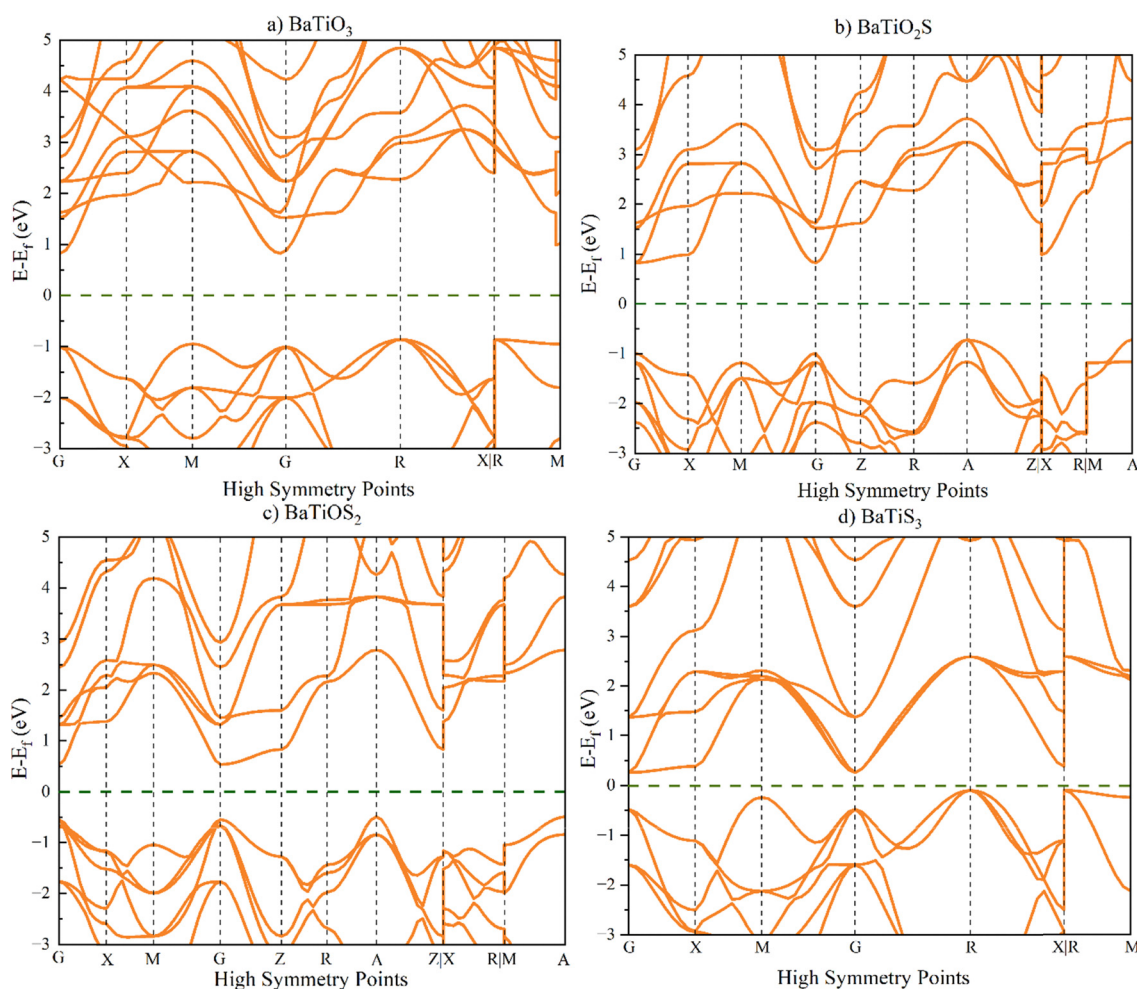
Table 2 Band gaps of $BaTiO_{3-x}S_x$ compounds

Compounds	Approach	Bandgap (eV)	Ref.
$BaTiO_3$	GGA–PBE	1.7002	This study
	HSE06	3.0691	This study
	Experimental	3.12	23
$BaTiO_3$ (SC)	GGA–PBE	1.7053	This study
	HSE06	3.1064	This study
$BaTiO_2S$	GGA–PBE	0.6157	This study
	HSE06	1.5501	This study
$BaTiO_2S$ (SC)	GGA–PBE	0.6133	This study
	HSE06	1.5501	This study
$BaTiOS_2$	GGA–PBE	0.2570	This study
	HSE06	1.0221	This study
$BaTiOS_2$ (SC)	GGA–PBE	0.2456	This study
	HSE06	1.0234	This study
$BaTiS_3$	GGA–PBE	0	This study
	HSE06	0.3542	This study
$BaTiS_3$ (SC)	GGA–PBE	0	This study
	HSE06	0.3307	This study

1.0221 eV. The bandgap remains indirect, with the VBM and CBM located at A and G points, respectively. In $BaTiS_3$ [Fig. 3(d)], where all O atoms are replaced by S, the band structure shows an indirect bandgap of 0.3542 eV. The VBM and CBM are located at R and G. The bandgap of the

$BaTiO_{3-x}S_x$ series decreases systematically with increasing S content, from 3.0691 eV for $BaTiO_3$ to 0.3542 eV for $BaTiS_3$. Sulfur's larger atomic size elongates the Ti–S bonds compared to the Ti–O bonds, thereby increasing lattice strain. Consequently, the conduction band minimum (CBM) is lowered, and orbital overlap is diminished. Moreover, the lower electronegativity of S shifts the valence band maximum (VBM) upward, thereby enhancing the charge-transfer efficiency. The electronic structure was gradually altered, and the band gap narrowed as a result of orbital hybridization and bond interactions influenced by these atomic variations. The Shockley–Queisser limit states that 1.4 eV is the ideal band gap for a single-junction solar cell operating under standard solar illumination.[62] This value maximizes the theoretical light-to-electricity conversion efficiency. Achieving the highest possible light-to-electricity conversion efficiency requires this range of band gap.[62–64] Thus, $BaTiO_2S$ exhibits a close value of 1.5501 eV, which is promising for solar cell use. These possible changes in the electronic properties could benefit solar cells. The band gap was calculated for $BaTiO_2S$ and $BaTiOS_2$ using both the GGA and HSE06 functionals in the 112 (tetragonal) supercell (SC) method. The results from both approaches are

Fig. 3 Band structure of (a) $BaTiO_3$, (b) $BaTiO_2S$, (c) $BaTiOS_2$, and (d) $BaTiS_3$ compounds.

consistent, as shown in Table 2, supporting the accuracy of the findings.

From the study of DOS of $BaTiO_{3-x}S_x$, the alteration of the electronic structure can be seen due to successive S substitution. The contribution of the 2p state in the valence band (VB) is shown by the perfect alignment of the first peak in the total density of states (TDOS) with the 2p state of oxygen (O). Meanwhile, the first peak of the conduction band in the TDOS corresponds to the 3d state of titanium (Ti). The contribution of the 2p state of O decreases when sulfur (S) is substituted; however, a decrease in the band gap is observed due to hybridization between the 3p states of S, the 2p state of O,

and the 3d state of Ti. Fig. 4(a) depicts the DOS for $BaTiO_3$, where the valence band (VB) region is dominated by strong O 2p states in the region from −6 to −1 eV, while the conduction band shows sharp Ti 3d character above 2 eV, jointly accounting for the indirect bandgap value of 3.07 eV for the material. This configuration is drastically changed when sulfur is added to $BaTiO_2S$ [Fig. 4(b)]. The S 3p states become distinct peaks around −1 eV, which hybridize with the remaining O 2p and Ti 3d orbitals to cause the VB maximum to shift upward and the bandgap to decrease to 1.55 eV. The VB edge near E_f is nearly controlled by the S 3p orbitals in the case of $BaTiOS_2$ [Fig. 4(c)], which severely weakens the original O 2p contributions and
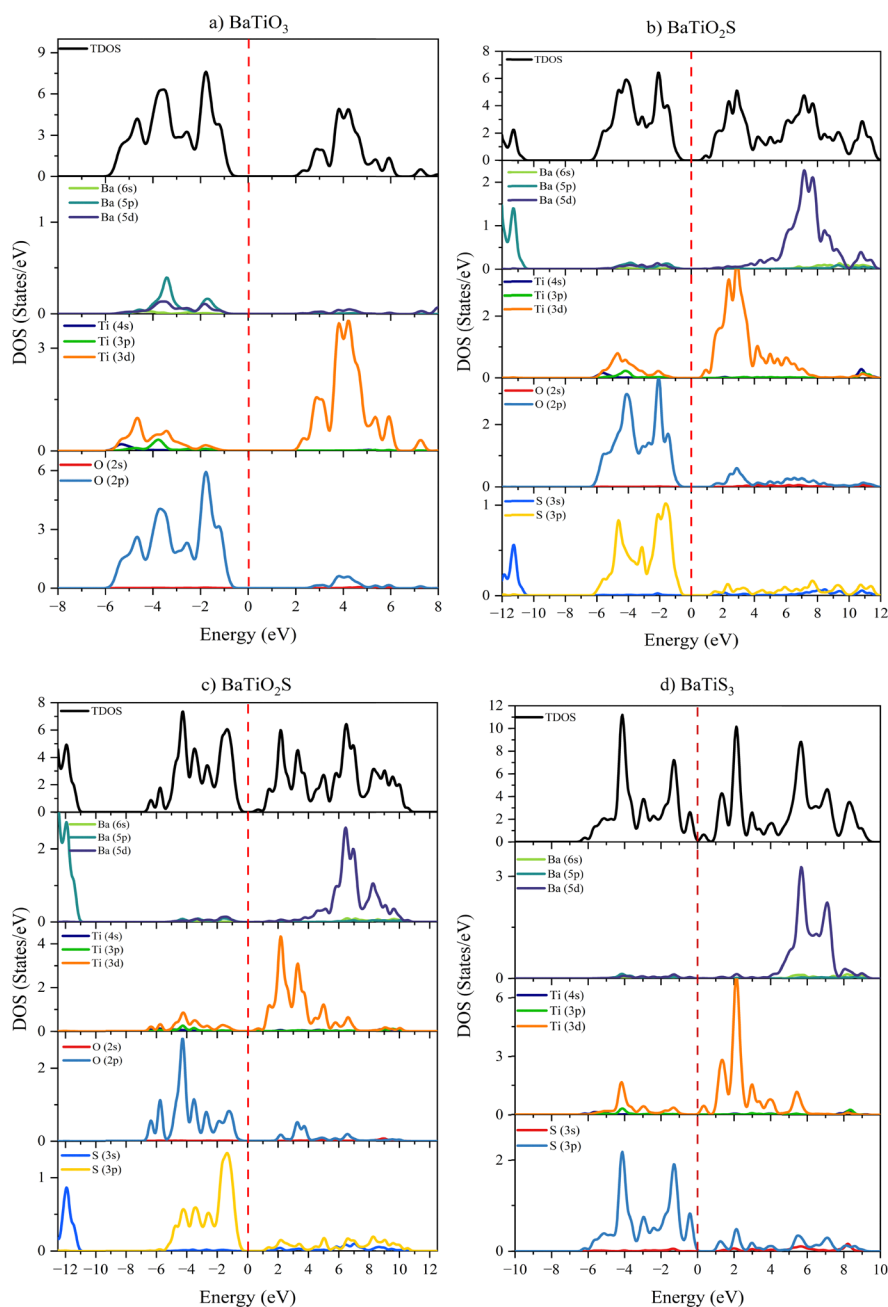

Fig. 4 The density of states (TDOS and PDOS) for (a) $BaTiO_3$, (b) $BaTiO_2S$, (c) $BaTiOS_2$, and (d) $BaTiS_3$ compounds.

further sharpens the gap down to 1.02 eV because of higher Ti 3d–S 3p interactions. The electronic structure of fully substituted $BaTiS_3$ can be seen in Fig. 4(d); the VB now only contains S 3p states, which greatly overlap with E_f, while the CB shows strong mixing between the Ti 3d and S 3p orbitals, resulting in a significantly smaller gap of 0.35 eV, which is near metallic. The observed band-gap narrowing with an increase in S quantity is a consequence of the anion electronic structure: S-3p states lie at higher energy than O-2p states and hence, by stronger S-3p/Ti-3d hybridization, raise the valence-band maximum. The projected density of states shows increasing S-3p at the top of the valence band as the value of x increases, while the electron charge density mapping illustrates enhanced shared electron density along Ti–S bonding directions, also signaling an increase in covalency. Both of these effects lower the photon energies at which optical transitions can occur, resulting in the progressive redshift of the absorption observed as one proceeds down the $BaTiO_3 \rightarrow BaTiO_2S \rightarrow BaTiOS_2 \rightarrow BaTiS_3$ series.

The band gap narrowing from UV (3.07 eV in $BaTiO_3$) through the visible region (1.02–1.55 eV in $BaTiO_2S/BaTiOS_2$) to near-IR (0.35 eV in $BaTiS_3$) demonstrates that the S acts primarily to uplift the VB to higher energy due to S 3p state insertion while maintaining the basic Ti 3d character of the CB. Since their ideal band gaps (around the Shockley–Queisser limit of 1.4 eV) suggest that they are highly beneficial in visible-light harvesting applications, these intermediate compositions are of particular interest. Of course, pure $BaTiO_3$ and $BaTiS_3$ terminate this tunability for UV and IR technologies, respectively. Through controlled S substitution, materials for particular optoelectronic applications can be designed with the help of this orbital-level understanding of the DOS evolution.

The charge density distributions of pure $BaTiO_3$ and its S-doped derivatives, $BaTiO_2S$, $BaTiOS_2$, and $BaTiS_3$, were studied to gain a better understanding of changes in chemical bonding and electronic localization as S substitution increases. The screened hybrid HSE06 functional was employed to accurately capture nonlocal exchange effects, which are critical for modelling charge density in systems with mixed ionic–covalent bonding. The investigations were conducted across various crystallographic planes to determine how charge delocalization and bonding properties change with increasing S concentration. This is demonstrated by charge density contour plots in Fig. 5, which show the slow transition from ionic–covalent bonding in $BaTiO_3$ (Ti–O) to weaker, more ionic interactions in S-doped compounds (Ti–S). The addition of S causes a significant alteration in those surrounding the Ti–S and Ba–S bonds, where charge buildup is indicative of increased orbital hybridization and electronic localization. Fig. 5(a) illustrates the charge density of $BaTiO_3$ along the (110) plane. This indicates a higher degree of covalent bonding character due to the intensive and symmetric charge buildup between the Ti and O atoms. The relatively high charge density values within the Ti–O bond and the concentrated charges surrounding the O atoms indicate a situation in which the high electronegativity of O virtually controls the bond's polarity. Conversely, Ba atoms have nearly minimal charge interaction

with their environment, suggesting that their lattice interactions are ionic. When S replaces one O atom in $BaTiO_2S$ [Fig. 5(b) and (c)], the charge distribution starts to change, especially around the S atoms. In contrast to Ti–O, the charge density contours of the Ti–S bonds are broader and less intense, indicating weaker covalent bonding and stronger ionic interactions. This shift is explained by S's higher atomic radius and lower electronegativity compared to O. The localized effect of partial anionic substitution is evident in the more diffuse charge density surrounding S and the development of bonding asymmetry between Ti–O and Ti–S. As illustrated in Fig. 5(d) and (e), the effect becomes more pronounced as the substitution of $BaTiOS_2$ increases. Two S atoms have now coordinated the Ti atom, and the charge density will continue to delocalize in these regions. Compared to Ti–O in $BaTiO_3$ or $BaTiO_2S$, the Ti–S bonding seems weaker and more spatially stretched, and has notably lower peak charge densities.

In addition to weakening covalent bonds, this slow delocalization of charge also indicates structural and electrical changes in the bonding environment surrounding the Ti center as the anionic framework shifts. Finally, the (110) charge density map of totally substituted $BaTiS_3$ [Fig. 5(f)] exhibits an even and extremely low charge accumulation around the Ti–S bonds, with wider contours and a lack of bonding directivity. In contrast to its oxygen-rich counterparts, the S-rich combination exhibits a fundamental shift in its electronic structure, validating the previously observed ionic nature of bonding. The dielectric behavior, band structure, and possible catalytic activity of $BaTiO_3$ are all significantly impacted by the change from strong localized covalent bonding with Ti–O to a weaker, more ionic attachment of Ti to S.

3.3 Optical properties

The optical properties of a material are crucial for selecting suitable materials for optoelectronic and photovoltaic applications. They indicate the material's efficacy when interacting with light. The absorption coefficient is the most important optical measure, as it indicates how a substance absorbs light.[65] Electronic transitions in semiconductors are typically classified into two categories: intra-band transitions and inter-band transitions. Since interband transitions are crucial for establishing optical and transport features, they are typically given priority. However, because it allows the material to behave in a completely metallic manner within its band structure, the intra-band transition is also quite significant.[66] To explore how S substitution influences light–matter interaction, the optical properties of the $BaTiO_{3-x}S_x$ system were comprehensively studied. Key optical parameters were calculated using first-principles methods based on the HSE06 hybrid functional, providing detailed insight into optoelectronic behavior.

3.3.1 Dielectric properties. The optical dielectric response of $BaTiO_3$ and S-substituted compounds ($BaTiO_2S$, $BaTiOS_2$, and $BaTiS_3$) was evaluated by the real ($\varepsilon_1(\omega)$) and imaginary ($\varepsilon_2(\omega)$) parts of the dielectric function, as depicted in Fig. 6(a) and (b), respectively. These parameters play a crucial role in comprehending how a material stores and dissipates
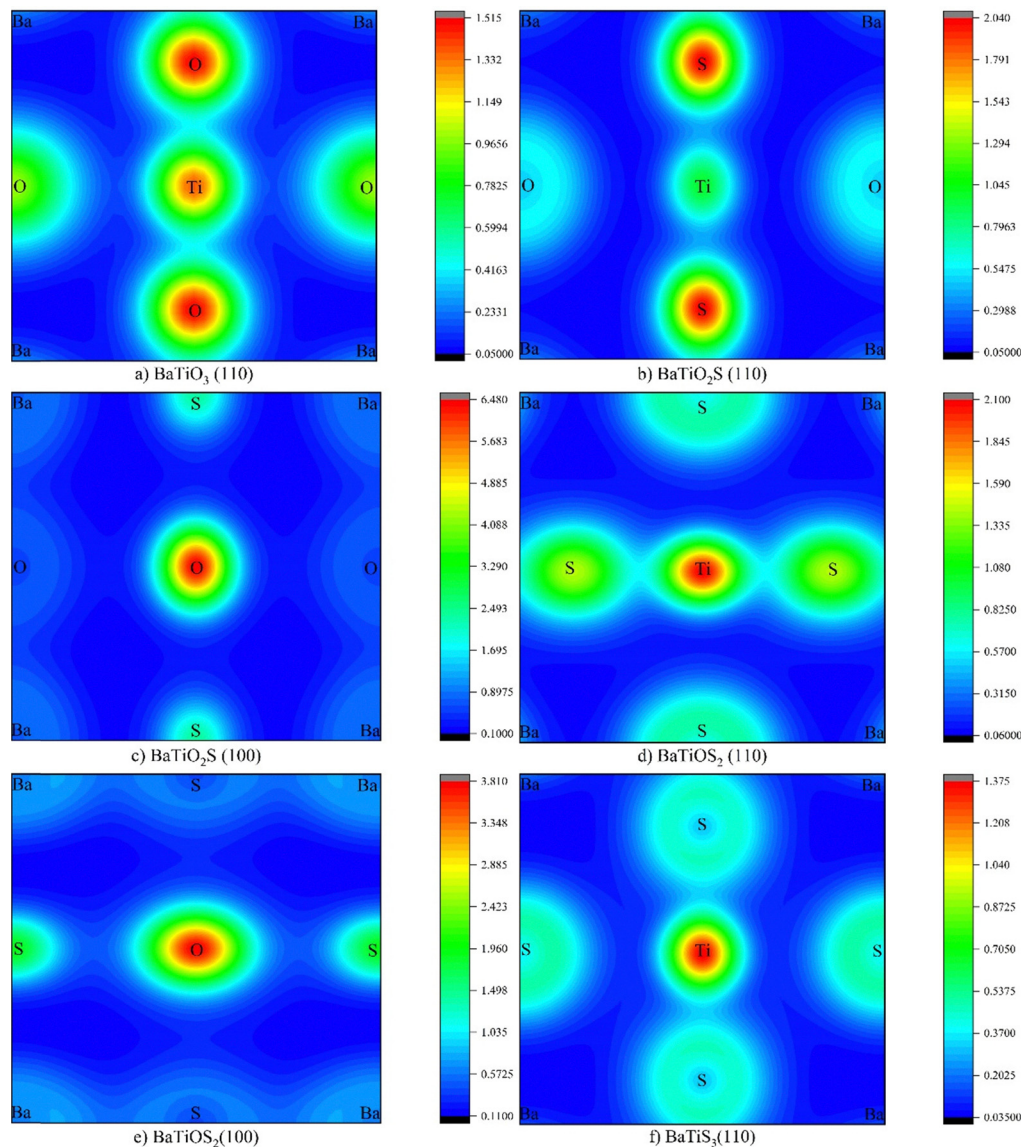
Fig. 5 2D Charge density plots for (a) $BaTiO_3$ (110), (b) $BaTiO_2S$ (110), (c) $BaTiO_2S$ (100), (d) $BaTiOS_2$ (110), (e) $BaTiOS_2$ (100), and (f) $BaTiO_3$ (110).

electromagnetic energy. The equation typically used to express the dielectric function is given below:[67]

$$\varepsilon(\omega) = \varepsilon_1(\omega) + i\varepsilon_2(\omega)$$

where ω denotes the angular frequency of the incident light. Collectively, $(\varepsilon_1(\omega))$ and $(\varepsilon_2(\omega))$ offer a comprehensive representation of a material's visual properties, which are ascertained by applying the Kramer's Kronig relation.[68]

In Fig. 6(a), the real part of the dielectric function $(\varepsilon_1(\omega))$ is related to photon energy. Of all compounds studied, $BaTiS_3$ has the greatest static dielectric constant $(\varepsilon_1(\omega)$ at 0 eV) with a value of 54.68 due to the relatively higher polarizability of S atoms compared with O atoms. This indicates that they can polarize more effectively in the presence of an external electric field. Again, both $BaTiO_2S$ (SC) and $BaTiOS_2$ (SC) exhibit a higher $\varepsilon_1(\omega)$ than pristine $BaTiO_3$, with values of 10.1, 31.124, and 9.6, respectively, suggesting that partial replacement of S might

increase dielectric screening. Further along, anisotropy in the xx and zz components is striking in the S-doped systems, as their anisotropic dielectric behavior is due to structural asymmetry and local distortions caused by S incorporation. The imaginary part of the dielectric function $(\varepsilon_2(\omega))$, which encompasses interband transitions and optical absorption characteristics, is presented in Fig. 6(b). Strong absorption peaks of $BaTiS_3$ [25.5] are found within the low-energy region (0.5–2.5 eV), signifying that those strong optical transitions, facilitated by its narrower band gap and modified electronic structure, are anticipated. Reinforced maximum $\varepsilon_2(\omega)$ values for $BaTiOS_2$ [17.7] and $BaTiO_2S$ [20.8], especially in the supercell configurations, further indicate heightened light absorption within the visible spectrum. Such enhancement is attributed to S-induced alterations in the density of states and transition matrix elements, which enable efficient photon-induced electronic excitations. On the other hand, the
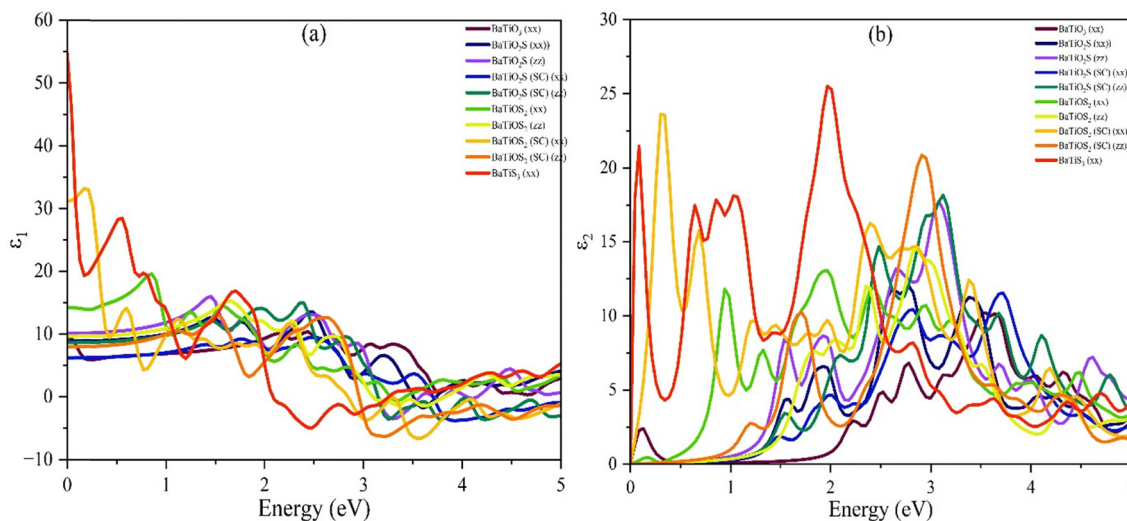
Fig. 6 Dielectric constant of BaTiO$_{3-x}$S$_x$ compounds: (a) real dielectric constant and (b) imaginary dielectric constant.

$\varepsilon_2(\omega)$ values of BaTiO$_3$, with the highest value of 10.3, are considerably lower, appropriate for a wide band gap, resulting in a decreased optical activity within the same energy range. It is very evidently clear now that S substitution enhances, in addition to the dielectric response, optical absorption. However, the scope of their investigation is limited to the significant increase in either $\varepsilon_1(\omega)$ or $\varepsilon_2(\omega)$, particularly BaTiS$_3$ and BaTiOS$_2$ (SC). Such indications suggest that S-doped BaTiO$_3$-based perovskites are promising materials for high-permittivity devices and optoelectronic applications, such as capacitors, photovoltaics, and photodetectors. The Penn model provides an empirical formulation for describing the dielectric function of semiconductors. The approximation of a nearly free-electron model simplifies the complexity of scattering processes in a semiconductor. The method enables us to calculate the dielectric constant, a crucial quantity for investigating a material's response to electromagnetic radiation, thereby enhancing our understanding of how a semiconductor behaves optically and its electronic structure.[69] The values described earlier meet those mentioned by the Penn model, to which the following equation is valid:[70]

$$\varepsilon_1(0) \approx 1 + \left[\frac{\hbar\omega_p}{E_g}\right]^2$$

At higher energies, however, the dielectric function tends to turn negative, revealing metallic behavior due to electron transition.[5]

3.3.2 Absorption coefficient. The optical absorption coefficient, $\alpha(\omega)$, is a critical parameter that determines the efficacy of solar energy conversion and measures the extent to which light of a specific wavelength is absorbed per unit length within the optical medium.[71] At the atomic scale, optical absorption occurs when incoming photons have a frequency that matches the energy of the electronic transition. Consequently, materials with a higher $\alpha(\omega)$ facilitate more efficient electron transitions

from the valence band to the conduction band. The absorption coefficient, $\alpha(\omega)$, is given by the following equation:[72]

$$\alpha(\omega) = \left[\sqrt{\varepsilon_1^2(\omega) + \varepsilon_2^2(\omega)} - \varepsilon_2(\omega)\right]^{\frac{1}{2}}$$

Fig. 7(a) depicts the absorption coefficient $\alpha(\omega)$, which relates to the material's ability to absorb incoming photons between 0–5 eV energies. BaTiO$_3$ shows a fairly high absorption onset around 3.1 eV, consistent with a large optical band gap. However, the presence of S substitution significantly redshifts the absorption edge for all doped compounds, particularly for BaTiO$_2$S (SC), BaTiO$_2$S (SC), and BaTiS$_3$, indicating considerable band gap narrowing and increased absorption capacity in the visible range. BaTiO$_2$S [5.45×10^5] demonstrates a shift of the absorption edge toward lower photon energies ($\sim$2.7 eV), characteristic of band gap reduction and enhanced absorption in the visible range. The absorption further increases in the BaTiOS$_2$ [7.25×10^5] and BaTiOS$_2$ (SC) [9.04×10^5] structures, exhibiting stronger and broader absorption features that extend well into the visible spectrum (1.5–3.5 eV). For all the systems under consideration, BaTiS$_3$ shows an exceptionally high absorption intensity of more than 9.16×10^5 cm^{-1} in the visible region, strongly indicating its highest potential for photon harvesting. BaTiS$_3$ and BaTiOS$_2$ (SC) display strong absorption bands in the 1.8–3.1 eV range, corresponding to S 3p → Ti 3d transitions enabled by the S-modified density of states near the Fermi level. Additionally, there is a clear anisotropy in the spectra for $\alpha(\omega)$, especially in the supercell configurations, where the optical response differs significantly between the xx and zz crystallographic directions. This anisotropic behavior arises from the symmetry-breaking effect of the S substitutions and the lattice distortions, which change the electronic dipole transition probabilities.

3.3.3 Optical reflectivity. The optical reflectivity $R(\omega)$, therefore, characterizes the ratio of reflected light to incident
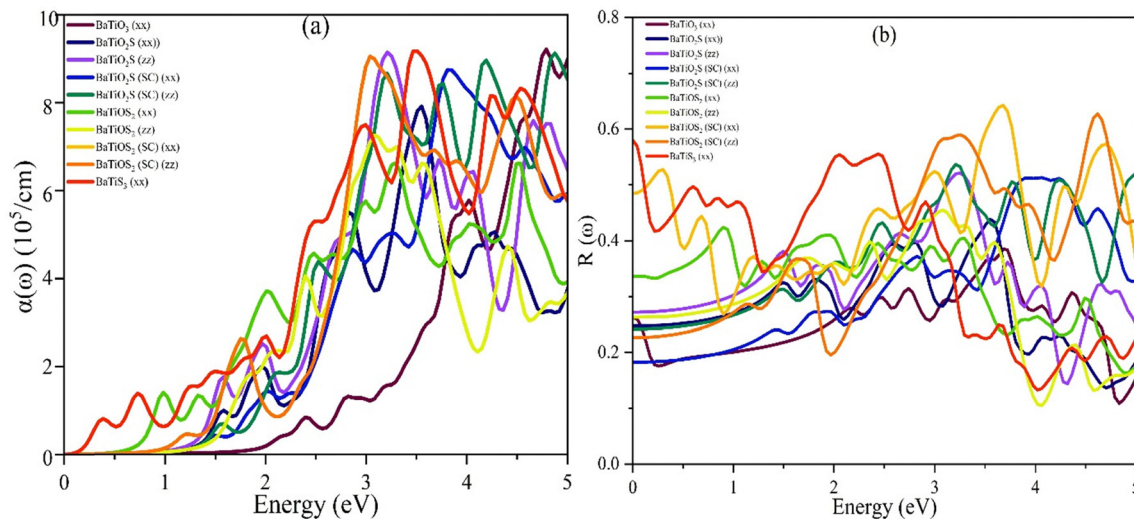
Fig. 7 (a) Absorption coefficient and (b) optical reflectivity of $BaTiO_{3-x}S_x$ compounds.

light and yields insight into the capacity of a material to reflect photons when they reach the surface. The reflectivity spectra $R(\omega)$ for the same series of compounds over the photon energy range are presented in Fig. 7(b). $BaTiO_3$ exhibited nearly low reflectivity values (<0.3) throughout the studied spectrum, whereas $BaTiS_3$ and $BaTiOS_2$ (SC) in the low-energy region showed very high optical reflectivity values over 0.6, correlating with hybrid S 3p–Ti 3d transitions and, thus, indicating good possibilities for use in reflection or photon-coating layers. Although S-substituted systems exhibit significantly enhanced reflectivity, $BaTiO_2S$ and $BaTiO_2S$ (SC) show relatively low reflectivity, as low as 26% in the visible region (1.8–3.1 eV), which is very promising for photoactive materials in visible-light-driven devices such as solar cells, photodetectors, or photocatalysts. The dichotomy of high reflectivity in S-rich compounds and low reflectivity in intermediate compositions emphasizes the tunable nature of the $BaTiO_{3-x}S_x$ material

system towards applications in reflective coatings (such as $BaTiS_3$) and light-harvesting devices (such as $BaTiO_2S$).

3.3.4 Energy loss function. The energy loss function $L(\omega)$, which quantifies plasmonic excitations and energy dissipation by fast electrons, reveals distinct trends across the $BaTiO_{3-x}S_x$ series,[73] as shown in Fig. 8(a). $BaTiO_3$ exhibits a low and broad $L(\omega)$, with most energy loss peaks appearing at higher photon energies beyond 4 eV due to its large band gap and low free carrier density. The intermediate compound $BaTiO_2S$, lying between the oxide and fully S-substituted phases, shows a more structured energy loss response compared to $BaTiO_3$. In both the xx and zz directions, $BaTiO_2S$ displays peaks in the 2–4 eV energy range, indicating the formation of low-energy collective electronic excitations (or plasmons). These features become more pronounced in the supercell model of $BaTiOS_2$, where localized lattice distortions and electron redistribution due to S incorporation strengthen the plasmonic activity. The highest
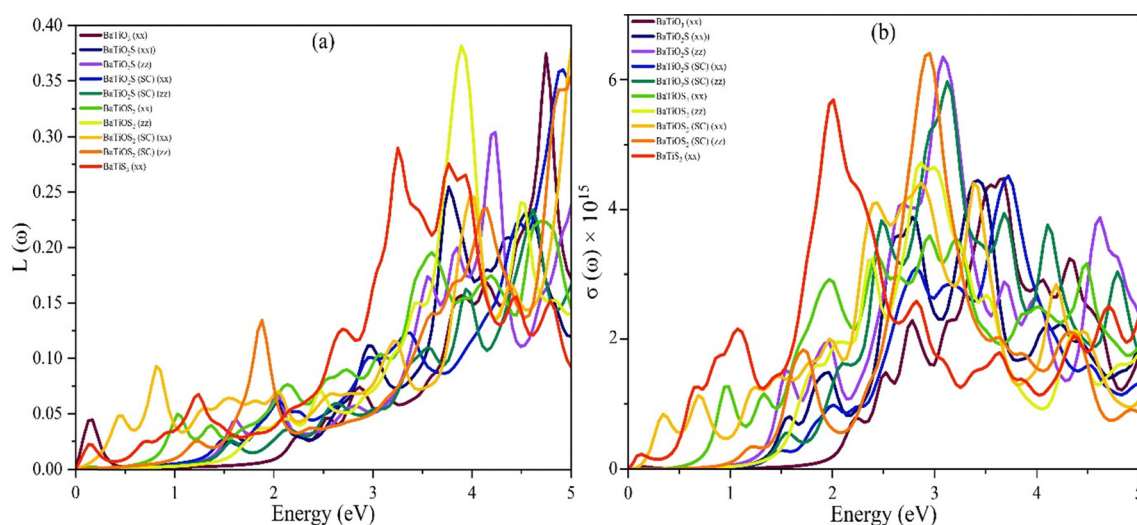

Fig. 8 (a) Loss function and (b) optical conductivity of $BaTiO_{3-x}S_x$ compounds.

energy loss intensity has been observed in BaTiS$_3$, which demonstrates sharp and dominating peaks, especially in the visible region (1.5–3.5 eV), attributed to the high density of states and enhanced polarizability introduced by the complete O-to-S substitution. In contrast to BaTiO$_3$, BaTiO$_2$S bridges the gap in plasmonic behavior, exhibiting insulating and conductive properties that render it suitable for tailoring optical applications.

3.3.5 Optical conductivity. The ability of the material to produce and transport photoinduced charge carriers is illustrated in Fig. 7(b), denoted $\sigma(\omega)$, based on the optical conductivity spectra.[37] BaTiO$_3$ shows very low optical conductivity in a range below 3 eV, which is consistent with its wide band gap, rendering it weakly optically active in the visible emission spectrum. BaTiO$_2$S exhibits much higher optical conductivity values, mainly in the low-energy region around 1.5–3 eV, with sharper peaks in its supercell configuration (SC). This increase can be attributed to the partial substitution of O^{2-} with S^{2-}, which decreases the band gap and generates shallow electronic states that permit more effective photoexcitation, thereby enhancing carrier mobility. The conductivity spectrum of BaTiO$_2$S (SC) reveals distinct peaks indicating considerable optical transitions, possibly due to hybridized Ti 3d and S 3p states. BaTiS$_3$ again demonstrates the highest optical conductivities across the entire range of photon energies, with maxima exceeding 6×10^{15} S^{-1}, indicating narrow band semiconducting behavior. Intermediate between the two extremes is BaTiO$_2$S, which presents a favorable balance between light absorption, moderate carrier mobility, and tunability through controlled incorporation of sulfur. The optical anisotropic behavior of BaTiO$_2$S and its derivatives, particularly in supercell modeling, underscores the importance of structural directionality for electronic transitions and dielectric response-concepts that are vital for the design of polarization-sensitive devices.

3.3.6 Extinction coefficient. The extinction coefficient $K(\omega)$, depicted in Fig. 9(a), describes the absorption and attenuation

of light inside the material. For BaTiO$_3$, $K(\omega)$ remains substantially low below 3 eV because it possesses a wide band gap and exhibits minimal absorption across various visible wavelengths. Absorption is significantly observed around 3 eV; thus, BaTiO$_3$ proves to be a transparent dielectric material. BaTiO$_2$S shows a clear increase in $K(\omega)$ compared to BaTiO$_3$ in the visible range of approximately 1.5–3.5 eV due to S substitution. This enhancement arises from the creation of intermediate energy states by S atoms and the lowering of the band gaps, which leads to improved visible light absorption. The supercell configuration of BaTiO$_2$S (BaTiO$_2$S-SC) demonstrates even more pronounced absorption features than those attributed to localized distortions and structural anisotropy. An increased S concentration in BaTiOS$_2$ and BaTiOS$_2$(SC) leads to an even greater rise in $K(\omega)$, suggesting stronger absorption across a broader energy range. These compounds also reconcile the optical behavior within systems exhibiting partial and full substitution. The highest extinction coefficient is observed in BaTiS$_3$, which displays one of the highest absorptions starting from photon energies as low as 0.5 eV, reaching peak $K(\omega)$ values exceeding 3.0 in the 2–3 eV energy range. This significant light attenuation can be attributed to the narrow band gap and strong electronic transitions from S 3p states to T 3d states, positioning BaTiS$_3$ as a favorable candidate for applications in visible light absorption.

3.3.7 Refractive index. Fig. 9(b) illustrates the refractive index $n(\omega)$, which describes how much the propagation of light is slowed inside the material. BaTiO$_3$ possesses quite a strong static refractive index of around ~ 2.5–3, which reduces with an increase in photon energy, following the normal dispersion behavior generally followed by wide-bandgap insulators. On the other hand, for BaTiO$_2$S, the static refractive index is slightly higher than that of BaTiO$_3$. It stays between 3 and 4 under visible photon energy, which indicates that the polarizability of the lattice is improved. The supercell configuration of BaTiO$_2$S (SC) has an even higher refractive index since S incorporation,

Fig. 9 (a) Reflective index and (b) extinction coefficient of BaTiO$_{3-x}$S$_x$ compounds.

in addition to local distortion effects, would help boost the optical density. For BaTiOS$_2$ and BaTiOS$_2$ (SC), the rise in the refractive index goes beyond 4, which is greater than for BaTiO$_3$ and BaTiO$_2$S, especially in the visible region. This indicates that there will be better light–matter interaction as a result of differences in dielectric constant, which are a function of the higher polarizability of sulfur atoms. The highest value was for BaTiS$_3$, and its static values exceeded 6.5 at all wavelengths and it possessed a very significant optical dispersion across the whole spectrum. Optoelectronic applications require refractive index values, $n(\omega)$, typically between 2.0 and 4.0,[74] which the investigated materials fulfil, surpassing the refractive index of silicon nitride (1.9), commonly used in solar cells.[75] High electronic polarizability, a low bandgap, and optical characteristics make these materials attractive for photonic and optoelectronic applications.

Fig. 10 illustrates the progressive changes in several key optical parameters of these materials as the S concentration increases in BaTiO$_3$, BaTiO$_2$S, BaTiOS$_2$, and BaTiS$_3$. Fig. 10(a) shows that the static dielectric constant $\varepsilon_1(0)$ and refractive index $n(0)$ both increase with S substitution, justifying enhanced polarizability and further engagement of light with matter. Fig. 10(b) depicts the maximum values of the absorption coefficient $\alpha(\omega)$ and optical conductivity $\sigma(\omega)$ in the visible region (1.6–3.1 eV); both display an increasing trend with higher S content, indicating that S enhances light absorption and carrier excitation. The onset of visible-range optical absorption and enhancements in $\varepsilon(0)$, $n(0)$, and the extinction coefficient have two interconnected origins: (i) the reduced electronic band gap discussed above, which enables low-energy interband transitions (particularly S-3p → Ti-3d), and (ii) the increased polarizability of S anions that raises the real part of the dielectric function. These electronic changes collectively increase the joint density of states and transition matrix elements within the visible energy range (1.6–3.1 eV). These trends collectively illustrate the favorable effects of S doping in

tailoring the optical properties of BaTiO$_3$-based compounds for visible-light optoelectronic applications.

3.4 Mechanical properties

This section discusses the mechanical characteristics of crystalline solids, which reflect their diverse reactions to various applied loads. This provides insights for predicting potential applications across different fields based on physical properties such as stiffness, fracture toughness, mechanical stability, elastic moduli, ductility, brittleness, hardness, and elastic anisotropy. The independent elastic constants were initially derived from strain-stress tests conducted in this study, thereby structuring the research on mechanical characteristics.[76] Crystal strain is related to its elastic stiffness, as it indicates structural and mechanical stability, as well as bonding characteristics. This behavior, however, is sometimes very hard to model because often accurate means to determine stress and damage model matching strain are needed. To assess the elastic properties of polycrystalline materials, the upper and lower values of the elastic moduli were calculated using Hill's approximation of the elastic constants.[77] The calculated elastic constants for S-doped BaTiO$_{3-x}$S$_x$ compounds are given in Table 3. The stability criteria for these cubic and tetragonal structures are given below:[78]

For cubic: $C_{11} - C_{12} > 0$, $C_{11} + 2C_{12} > 0$, and $C_{44} > 0$.

For tetragonal: $C_{11} > |C_{12}|$, $2 \times C_{13}^2 < C_{33}(C_{11} + C_{12})$, $C_{44} > 0$, and $C_{66} > 0$.

From Table 3, it can be seen that BaTiO$_{3-x}$S$_x$ compounds meet their specific aforementioned criteria, confirming their mechanical stability.

Mechanical properties of BaTiO$_{3-x}$S$_x$ compounds regarding their supercell (SC) arrangements have been calculated and presented in Table 4. These properties include bulk modulus
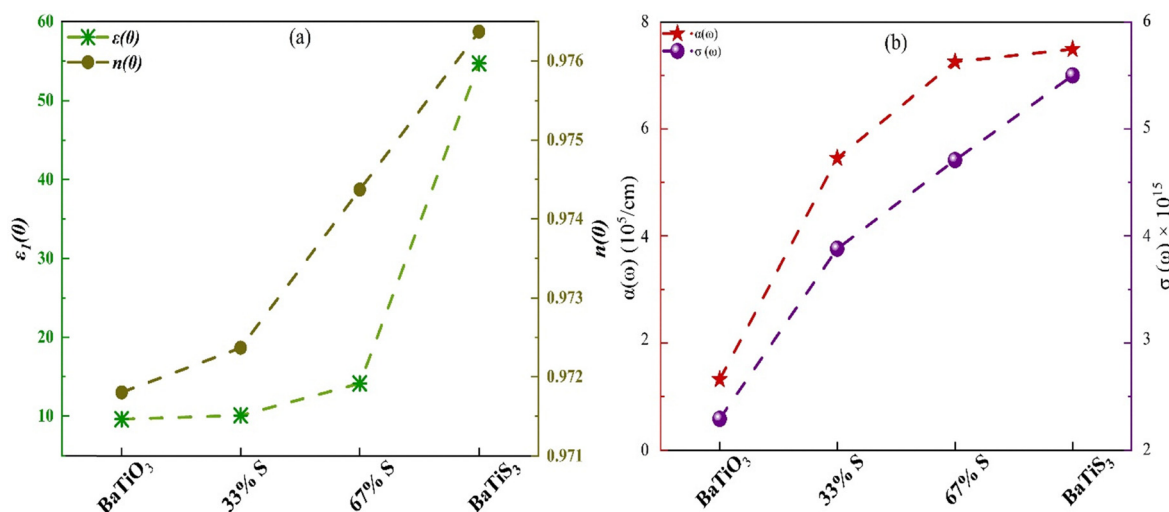

Fig. 10 Effect of sulfur doping on (a) static dielectric constant $\varepsilon_1(0)$ and refractive index $n(0)$ and (b) absorption coefficient $\alpha(\omega)$ and optical conductivity $\sigma(\omega)$.

Table 3 Calculated stiffness constants (GPa) of $BaTiO_{3-x}S_x$ compounds with cubic and tetragonal structures

Compound	C_{11}	C_{12}	C_{13}	C_{44}	C_{33}	C_{66}
$BaTiO_3$	226.272	83.112	—	107.999	—	—
$BaTiO_2S$	209.216	141.030	39.128	53.414	181.020	145.780
$BaTiO_2S$ (SC)	213.182	142.649	39.659	54.225	179.827	146.004
$BaTiOS_2$	155.566	37.002	53.476	68.558	247.394	35.335
$BaTiOS_2$ (SC)	149.992	35.326	52.184	67.586	248.307	34.589
$BaTiS_3$	120.038	50.407	—	38.189	—	—
$BaTiS_3$ (SC)	119.071	47.135	—	35.655	—	—

(B), shear modulus (G), Young's modulus (Y), B/G ratio, Poisson's ratio (ν), Vickers hardness (H_v), and B/C_{44} ratio. The bulk modulus (B) defines the material's resistance to change in volume under the application of pressure.[79] The shear modulus (G) connects the rigidity of a material and its resistance to shape change; some relate it to hardness.[80] Young's modulus (Y) is the principal mechanical parameter characterizing the resistance of a material to elastic deformation under uniaxial tensile stress.[81]

With increasing sulfur content, the bulk modulus (B) decreases. The maximum bulk modulus, 131 GPa, is exhibited by $BaTiO_3$, suggesting strong interatomic bonding. In contrast, $BaTiS_3$ shows a much lower value of 73 GPa, indicating reduced bonding due to S substitution. This softening in mechanical behavior is evidenced by the progressive decline in shear modulus (G) and Young's modulus (Y), which resist shape deformation and subsequently overall stiffness from $BaTiO_3$ to $BaTiS_3$. S weakens the bonding strength in the lattice due to its larger atomic size and lower electronegativity compared to oxygen. The effect of sulfur doping on bulk modulus, shear modulus, and Young's modulus is illustrated in Fig. 11(a). The B/G ratio indicates ductility; much higher values suggest very ductile behavior. $BaTiO_3$ is relatively low at 1.43, similar to a brittle material; however, $BaTiS_3$ has a significantly higher B/G value of 2.00, indicating a considerable improvement in ductility for a fully S-substituted compound. This trend suggests that Poisson's ratio also reflects the transition from brittle to ductile behavior with increased S content (ν). The value is 0.216 for $BaTiO_3$, but for $BaTiS_3$, the increase brings it to 0.286. Additionally, a higher Poisson's ratio indicates better plastic deformation capability and reduced brittleness. In principle, S doping therefore enhances the material's mechanical flexibility. The correlation between Poisson's ratio and the B/G ratio is

Table 4 Computed bulk modulus B (GPa), Young's modulus Y (GPa), shear modulus G (GPa), Pugh's ratio (B/G), Poisson's ratio ν, and machinability index B/C_{44} for $BaTiO_{3-x}S_x$ compounds

Compound	B	G	Y	B/G	ν	$(H_v)_{Chen}$	$(H_v)_{Tian}$	B/C_{44}
$BaTiO_3$	131	92	223	1.429	0.216	15.37	15.02	1.21
$BaTiO_2S$	112	67	168	1.66	0.258	9.86	10.16	2.11
$BaTiO_2S$ (SC)	113	68	170	1.66	0.25	10.01	10.29	2.10
$BaTiOS_2$	91	60	147	1.53	0.232	10.16	10.22	1.33
$BaTiOS_2$ (SC)	89	59	144	1.52	0.230	10.18	10.21	1.32
$BaTiS_3$	73	36	95	2.00	0.286	4.29	5.37	1.93
$BaTiS_3$ (SC)	72	36	92	1.99	0.285	4.23	5.31	1.98

illustrated in Fig. 11(b). Hardness testing is the fundamental basis in materials science, since hardness provides direct insight into resistance to deformation and wear, rendering it essential for assessing appropriateness for specific applications. Different hardness models enhance our comprehension of the in-ground mechanical behavior of materials, hence facilitating their selection and design for specialized applications. In this work, hardness predictions were made for $BaTiO_{3-x}S_x$ compounds using established approaches given by Tian *et al.*[82] and Chen *et al.*[83] Among the compounds studied, $BaTiO_3$ was found to be much harder than the other three.

S substitution leads to an increase in the B/C_{44} ratio, which gauges elastic anisotropy and bonding properties. $BaTiO_2S$ and $BaTiOS_2$ show intermediate values (~ 2.1 and $\sim 1.1.3$, respectively), while $BaTiS_3$ reaches $\sim 1.1.9$. In contrast, $BaTiS_3$ has a relatively low B/C_{44} ratio (1.21). This pattern suggests that the nature of interatomic interactions is altered and elastic anisotropy is enhanced by sulfur substitution. Sulfur substitution decreases the average bond stiffness since, on average, Ti–S bonds are softer than Ti–O bonds. The reduced stiffness arises from increased Ti–anion bond lengths and from more polarizable S ions, reducing resistance to deformation but enhancing mechanical compliance—an effect that is consistent with the observed increase in the B/C_{44} ratio[84] and with the CDM indicating more delocalized bonding for Ti–S. Overall, the findings demonstrate that S dopants consistently exert a stochastic effect, stressing the material to the point of damaging its mechanical stiffness while increasing its ductility and elastic anisotropy. S-substituted $BaTiS_3$ compounds will benefit from these mechanical modifications and enhanced optical characteristics, making them suitable for various applications in optoelectronic materials.

3.5 Thermal properties

Debye temperature (Θ_D) is fundamental for characterizing solids' vibrational properties and thermal behavior. On the other hand, it is related to the material's stiffness and sound velocity and tells us about lattice vibrations and phonon transport. The term "Debye temperature" was given in honor of Dutch physicist Peter Debye. It is the scale of temperature at which all possible atomic modes of vibration in a crystalline solid are excited.[85] Elevated Θ_D values indicate a more robust handling of atoms and a slight solidity in the structure.[86] The densities (ρ) and the longitudinal (ν_l), transverse (ν_t), average sound velocities (ν_m) and Debye temperatures (Θ_D) of $BaTiO_{3-x}S_x$ compounds are computed and displayed in Table 5. $BaTiO_3$ has strong interatomic bonding and stiffness, as evidenced by its maximum sound velocities ($\nu_l = 6710$ m s^{-1}, $\nu_t = 4038$ m s^{-1}, and $\nu_m = 4465$ m s^{-1}) and a Θ_D of 555 K. Sound velocities and Debye temperatures steadily decrease as S gradually replaces O in the lattice ($BaTiO_2S \rightarrow BaTiOS_2 \rightarrow BaTiS_3$). The higher atomic mass of S, accompanied by the weaker bonding environment, is the reason for this decrease. Conversely, $BaTiS_3$ exhibits the lowest Debye temperature (350 K) and sound velocities ($\nu_m = 3329$ m s^{-1}), indicating a lower lattice
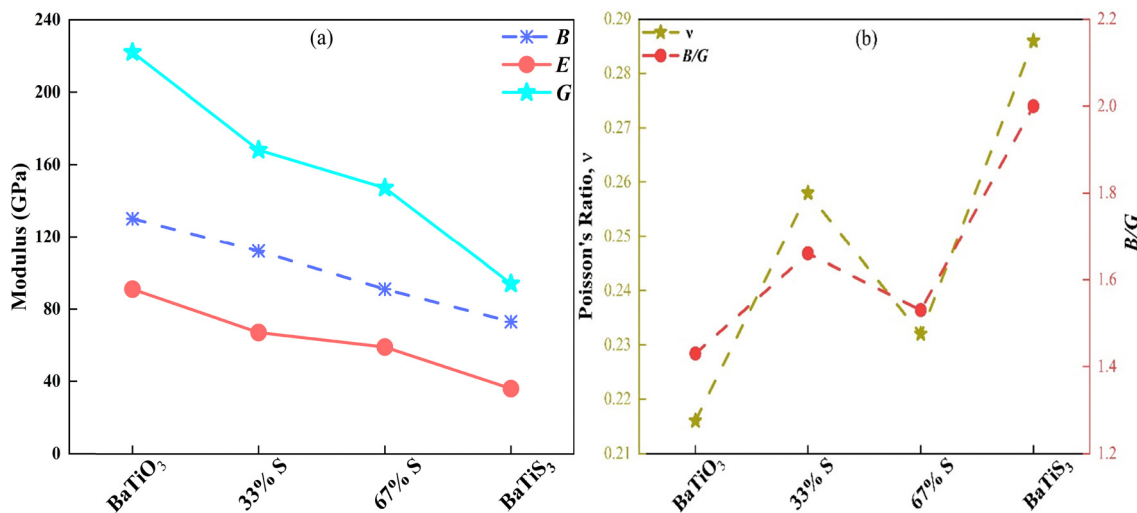
Fig. 11 Effect of sulfur doping on (a) elastic moduli and (b) Poisson's ratio and B/G.

Table 5 Calculated crystal density (ρ), transverse, longitudinal, and average sound velocities (ν_l, ν_t, and ν_m), and Debye temperature (Θ_D) for BaTiO$_{3-x}$S$_x$ compounds

Compound	ρ (kg m^{-3})	ν_l (m s^{-1})	ν_t (m s^{-1})	ν_m (m s^{-1})	Θ_D (K)
BaTiO$_3$	6240	6710	4038	4465	555
BaTiO$_2$S	5000	6353	3670	4074	476
BaTiOS$_2$	4230	6158	3637	4030	445
BaTiS$_3$	4130	5451	2986	3329	350

and phonon energy scale. From the trend, it can be said that substitution enervates the lattice while lowering the Debye temperature and acoustic phonon velocities, which in turn affect these materials' anharmonic properties and thermal conductivity.

The melting temperature of the BaTiO$_{3-x}$S$_x$ compounds was calculated using $T_m = [553 + (5.911)C_{11}]$ for the cubic phase and $T_m = 3C_{11} + 1.5C_{33} + 354$ for the tetragonal phase.[87,88] From Table 6, it can be observed that the melting temperature (T_m) decreases from BaTiO$_3$ (1890.5 K) to BaTiOS$_2$ (1192 K), indicating a decrease in thermal stability with an increase in S concentration in the lattice. The comparatively higher T_m values for BaTiO$_3$ imply strong bonding and, thus, thermal resistance, whereas the lower values for sulfur-rich compounds may suggest weak lattice cohesion.

The Grüneisen parameter (γ), which measures both anharmonicity and thermal expansion aspects, exhibits a decreasing

Table 6 Calculated melting temperature (T_m), Grüneisen parameter (γ), lattice thermal conductivity (K_{ph}), specific heat (C_v, C_p), and Gibbs free energy of BaTiO$_{3-x}$S$_x$ perovskite compounds

Compounds	T_m (K)	γ	K_{ph} (W mK^{-1})	C_v	C_P	S (J K^{-1} mol^{-1})
BaTiO$_3$	1890.5	1.35	5.48	98.6	99.1	108.57
BaTiO$_2$S	1253	1.54	3.92	92.2	92.6	110.06
BaTiOS$_2$	1192	1.42	1.23	106.2	107.2	138.67
BaTiS$_3$	1262	1.69	1.18	83.7	83.8	149.91

trend from 1.35 in BaTiO$_3$ to 1.69 in BaTiS$_3$, as shown in Table 6. This increase demonstrates how phonon–phonon scattering is enhanced by the rise in S content, leading to a decrease in lattice thermal conductivity. The Grüneisen parameter (γ) was calculated using the following formula, where ν is Poisson's ratio.

$$\gamma = \frac{3(1+\nu)}{2(2-3\nu)}$$

The ability of a solid material to transfer heat through the vibrations of its atoms (phonons) is known as lattice thermal conductivity. From Fig. 12, it can be seen that the highest K_{ph} is found in BaTiO$_3$, which shows effective phonon transport because of its strong bonding and low anharmonicity. It starts above 50 W m^{-1} K^{-1} at low temperatures and stays around 1.713 W m^{-1} K^{-1} at 1000 K. BaTiO$_2$S exhibits decreased thermal conductivity ($\sim$25 W m^{-1} K^{-1} at 50 K) upon partial S substitution, with the xx direction being marginally less conductive than the zz direction. This is an indication of increased phonon scattering from mass disorder and lattice distortion. Both components decrease more significantly for BaTiOS$_2$, particularly in the xx direction, which at high temperatures drops around 0.367 W m^{-1} K^{-1}, suggesting strong phonon localization and anisotropy. With values falling below 5 W m^{-1} K^{-1} even at low temperatures and approaching the amorphous limit 0.363 W m^{-1} K^{-1} by 1000 K, the fully substituted BaTiS$_3$ exhibits the lowest and almost isotropic K_{ph}. This is attributed to high lattice anharmonicity and strong phonon scattering due to S's heavier mass and weaker bonding. Lattice thermal conductivity at 300 K is given in Table 6.

The evaluation of thermal properties, including conductivity and heat capacity, is made possible by the scattering or decay processes. For more in-depth insights into the underlying phonon transport mechanisms in the BaTiO$_{3-x}$S$_x$ series, the phonon lifetimes as a function of phonon frequency were
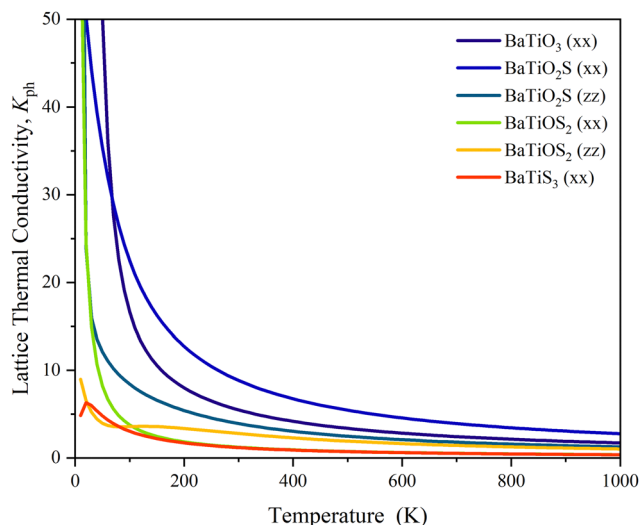
Fig. 12 Lattice thermal conductivity of $BaTiO_{3-x}S_x$ compounds.

considered (Fig. 13). There seems to be a correlation observed between the phonon lifetime distribution and the lattice thermal conductivity that is calculated (Fig. 12).[89] Phonon lifetimes, which go up to 1 ps or more in cleaner $BaTiO_3$ along the

phonon frequency around a mid-frequency region of 7–12 THz, indicate less strong phonon–phonon scattering and thus longer phonon mean free paths, leading to a higher value of lattice thermal conductivity. On the partial substitution of O with S, the phonon lifetimes get shorter in $BaTiO_2S$ and $BaTiOS_2$, particularly in the ranges of low and mid frequencies [Fig. 13(b) and (c)]. The enhanced scattering rates, with peak values above 0.20 and 0.35 ps^{-1}, respectively, may suggest increased phonon anharmonicities through mass disorder and bonding heterogeneities introduced by S atoms. The trend continues in fully substituted $BaTiS_3$ [Fig. 13(d)], where the shortest phonon lifetimes are mostly below 0.4 ps and maximum scattering rates of nearly 0.40 ps^{-1} are found, particularly in the low-frequency acoustic phonon region below 5 THz. These acoustic phonons mainly carry heat on a crystalline scale, and their strong damping suppresses lattice thermal conductivity. So, in connection with these phenomena, the observed progressive reduction in phonon lifetimes moving from $BaTiO_3$ to $BaTiS_3$ aligns with the change in lattice thermal conductivity across the series as presented in Fig. 13. This conclusion affirms that an S substitution in $BaTiO_3$ indeed serves to modulate phonon dynamics by increasing phonon scattering, subsequently reducing lattice thermal conductivity. The figure

Fig. 13 Lifetime vs. phonon frequency curve for (a) $BaTiO_3$, (b) $BaTiO_2S$, (c) $BaTiOS_2$, and (d) $BaTiS_3$ compounds.

of merit of thermoelectric materials depends directly on the electrical conductivity and inversely on the lattice thermal conductivity. The electronic properties section reveals the enhancements of electrical conductivity (by reducing the band gap), and this section reveals a reduction of lattice thermal conductivity. This combined effect could increase the thermoelectrical properties of S-rich compositions (BaTiS$_3$). The tunable thermal transport properties of the BaTiO$_{3-x}$S$_x$ system may find use in advanced heat management systems for microelectronic and optoelectronic devices.

The dramatic decrease in lattice thermal conductivity upon S substitution (K_{ph}: 5.48 → 1.18 W m^{-1} K^{-1}) is explained by two primary mechanisms. First, the greater mass of S (relative to O) reduces phonon group velocities through decreasing mean sound velocities (ν_m from 4465 → 3329 m s^{-1}) and reduced Debye temperatures (Θ_D from 555 → 350 K). Second, the increased lattice anharmonicity—represented by the higher Grüneisen parameter (γ rises from 1.35 → 1.69)—and mass/force-constant disorder introduced by mixed anions greatly increase phonon–phonon and impurity

scattering, shortening the phonon mean free paths and lowering κ. The accompanying vibrational entropy increase also favors stronger phonon scattering and anharmonicity in S-rich compounds.

3.5.1 Gibbs free energy, entropy, and specific heat. For BTiO$_{3-x}$S$_x$ compounds, Fig. 14 illustrates the temperature-dependent thermodynamic properties: Gibbs free energy (G), entropy (S), and specific heat at constant volume (C_v). These parameters shed light on the compounds' vibrational behavior and thermal stability over a temperature range of 0–1000 K.

The red curves represent the Gibbs free energy, which decreases as the temperature rises. The compounds' enhanced thermodynamic favorability at higher temperatures, due to entropy contributions, is reflected in this trend. Compared to its S-substituted counterparts, BaTiO$_3$ shows the highest thermodynamic stability at low temperatures, as evidenced by its most negative G values. The G values become less negative as the S content increases, indicating a slight decrease in thermal stability as S replaces O. This aligns with the lower stiffness and weaker bonding of the mechanical properties.
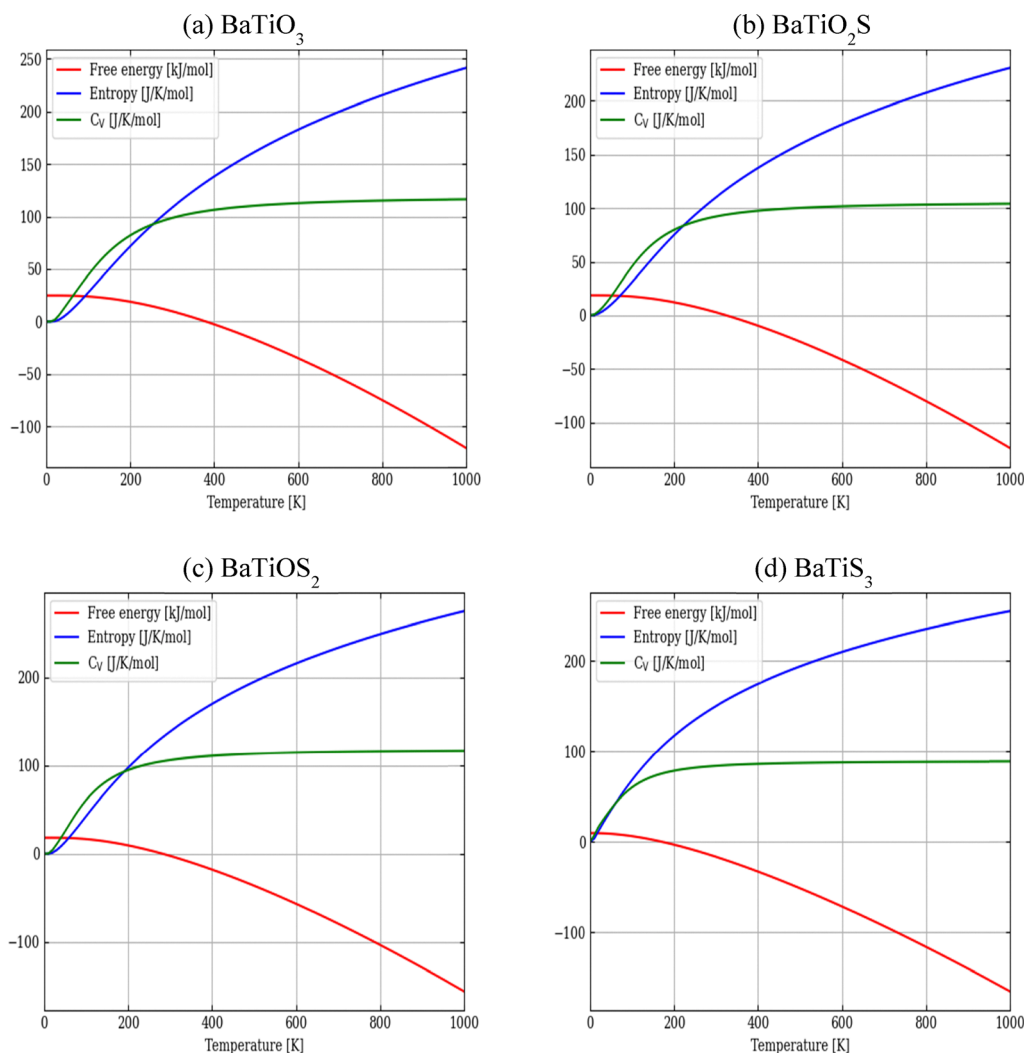

Fig. 14 Gibbs free energy, entropy, and specific heat at constant volume for (a) BaTiO$_3$, (b) BaTiO$_2$S, (c) BaTiOS$_2$, and (d) BaTiS$_3$ compounds.

Entropy (blue curves) increases smoothly with temperature for all materials. Because S atoms contribute additional atomic mass and vibrational degrees of freedom, the entropy magnitude is slightly higher in S-rich compositions ($BaTiOS_2$ and $BaTiS_3$). $BaTiO_3$ exhibits a somewhat lower value of ~ 215 J K^{-1} mol^{-1} at 1000 K, whereas $BaTiS_3$ reaches about 225 J K^{-1} mol^{-1}. This indicates that S substitution enhances the system's configurational entropy and vibrational disorder.

At low temperatures, the specific heat at constant volume (green curves) rises quickly, and at higher temperatures (above 600 K), it saturates near the Dulong–Petit limit (~ 125 J K^{-1} mol^{-1}). This behavior aligns with Debye theory, which posits that as the vibrational modes fill up, C_v tends to stabilize. Despite compositional differences, the C_v curves for all four compositions converge at high temperatures, suggesting comparable high-temperature phonon contributions. Although slight variations exist at low temperatures, $BaTiS_3$ displays a marginally higher C_v rise at early temperatures, likely due to S-induced low-frequency vibrational modes. Specific heat at constant pressure (C_p) was calculated using the formulas below:[90]

$$C_p = C_v(1 + \alpha \gamma T), \quad \text{where } \alpha = \frac{\gamma C_v}{3 B_t v_m}$$

Here, B_t represents the isothermal bulk modulus and v_m represents the molar volume. The values of C_v, C_p and entropy at 300 K are shown in Table 6.

According to thermal analysis, S substitution in the $BaTiO_{3-x}S_x$ compounds systematically lowers thermal conductivity by 40–60% while increasing vibrational entropy and heat capacity by 25–30% and 15–20%, respectively, due to improved phonon scattering and bond anharmonicity brought about by softer Ti–S bonds. The combination of ultralow thermal conductivity (~ 1.5 W m^{-1} K^{-1} in $BaTiOS_3$), high entropy, and strong anharmonicity makes S-rich phases particularly promising for thermoelectric applications where phonon suppression is crucial, as well as for thermal management in optoelectronic devices requiring temperature-stable operation, even though S incorporation slightly reduces thermodynamic stability (less negative formation energies). These patterns show how controlled S doping can engineer thermal transport properties without sacrificing structural integrity, providing a materials design pathway for energy conversion and heat regulation technologies.

4. Conclusions

The effect of S substitution on the mechanical, thermal, and opto-electronic properties of $BaTiO_3$ perovskite was thoroughly investigated by the DFT method, wherein substitution of O by S converts $BaTiO_3$ into $BaTiO_2S$, $BaTiOS_2$, and eventually $BaTiS_3$. All compounds exhibit negative formation energies and acceptable values of tolerance factors, and negligible fluctuation of energy (AIMD studies) confirmed the thermodynamical stability of the studied compositions. Partial substitution creates tetragonal distortions due to mixed Ti–O and Ti–S bonding, with the cubic-like phase becoming the ground-state structure

in $BaTiS_3$. Due to the significantly higher energy of S 3p orbitals compared to O 2p orbitals, sulfur doping effectively reduces the bandgap from the ultraviolet (3.06 eV) to the visible range (1.55 eV and 1.02 eV), thus rendering the compounds more suitable for solar and photocatalytic applications. The sulfur-incorporated absorbance edge undergoes a redshift with an increase in absorption coefficient (9.16×10^5 cm^{-1} in $BaTiS_3$), dielectric constant, refractive index, extinction coefficient (~ 0.55), and optical conductivity (up to $\sim 10^{15}$ S m^{-1}) in the visible-light range, bolstering suitability for photonic applications, photovoltaic absorbers, minimal photon loss, and excellent carrier transport capabilities. With increased S content, the elastic modulus and stiffness decrease, but ductility improves with higher B/G ratios (1.43 to 2.00) and Poisson's ratios (0.216 to 0.286), suggesting weakening of the Ti–S bonds and increased ductility. Hardness concurrently diminishes, indicating that sulfur-rich compositions are softer and more easily processed. As the atomic mass of S grows and lattice stiffness diminishes, the Debye temperature decreases from 555 K to 350 K for $BaTiO_3$ to $BaTiS_3$. The lattice vibration thermal conductivity, k_{ph}, drops substantially from 5.48 W m^{-1} K^{-1} to 1.18 W m^{-1} K^{-1} at 300 K due to increased phonon scattering caused by mass disorder and bond anharmonicity. Consequently, S doping results in higher specific heat and entropy, reflecting increased vibrational activity and thermal stability. Thus, S doping provides a controlled approach for engineering $BaTiO_{3-x}$ based perovskites with distinct properties in thermal, mechanical, and optoelectronic domains, thereby enhancing their potential in diverse areas.

Author contributions

U. Ahmed: data curation, investigation, visualization, formal analysis, and writing – original draft. M. M. Hossain: formal analysis, validation, writing – review and editing. M. M. Uddin: validation, writing – review and editing. N. Jahan: validation, writing – review and editing. M. A. Ali: conceptualization, methodology, formal analysis, validation, project administration, writing – review and editing, and supervision.

Conflicts of interest

The authors declare that they have no known competing financial interests or personal relationships that could have appeared to influence the work reported in this paper.

Data availability

The datasets generated during the current study are available from the corresponding authors upon reasonable request.

Acknowledgements

References

1 M. R. Mohaghegh, M. Heidari, S. Tasnim, A. Dutta and S. Mahmud, Latest advances on hybrid solar–biomass power plants, *Energy Sources, Part A*, 2021, **47**(1), 4901–4924.

2 J. Zeghlouli, G. Christophe, A. Guendouz, C. El Modafar, A. Belkamel and P. Michaud, *et al.*, Optimization of bioethanol production from enzymatic treatment of argan pulp feedstock, *Molecules*, 2021, **26**(9), 2516.

3 S. Mukherjee, S. Bin Mujib, D. Soares and G. Singh, Electrode materials for high-performance sodium-ion batteries, *Materials*, 2019, **12**(12), 1952.

4 Y. Nasr, H. El Zakhem, A. E. A. Hamami, M. El Bachawati and R. Belarbi, Comprehensive Review of Innovative Materials for Sustainable Buildings' Energy Performance, *Energies*, 2023, **16**(21), 7440.

5 S. Mahmud, U. Ahmed, M. A. U. Z. Atik, M. M. Hossain, M. M. Uddin and M. A. Ali, Novel $Cs_2Au^IM^{III}F_6$ (M = As, Sb) double halide perovskites: sunlight and industrial waste heat management device applications, *Phys. Chem. Chem. Phys.*, 2025, **27**(9), 4686–4703.

6 M. A. C. Teixeira, H. R. Ramos, A. Aguiar and O. e de, Perspectives of New Alternative Materials to Silicon for the Production of Photovoltaic Solar Cells, *Rev. Nac. Geren. Cid.*, 2021, **9**(71), 48–61.

7 M. Llanos, R. Yekani, G. P. Demopoulos and N. Basu, Alternatives assessment of perovskite solar cell materials and their methods of fabrication, *Renewable Sustainable Energy Rev.*, 2020, **133**, 110207.

8 W. Zhang, G. E. Eperon and H. J. Snaith, Metal halide perovskites for energy applications, *Nat. Energy*, 2016, **1**(6), 16048.

9 T. Islam, R. Jani, S. M. Al Amin, K. M. Shorowordi, S. S. Nishat and A. Kabir, *et al.*, Simulation studies to quantify the impacts of point defects: An investigation of $Cs_2AgBiBr_6$ perovskite solar devices utilizing ZnO and Cu_2O as the charge transport layers, *Comput. Mater. Sci.*, 2020, **184**, 109865.

10 S. Khatoon, S. Kumar Yadav, V. Chakravorty, J. Singh, R. Bahadur Singh and M. S. Hasnain, *et al.*, Perovskite solar cell's efficiency, stability and scalability: A review, *Mater. Sci. Energy Technol.*, 2023, **6**, 437–459.

11 J. Diekmann, P. Caprioglio, M. H. Futscher, V. M. Le Corre, S. Reichert and F. Jaiser, *et al.*, Pathways toward 30% Efficient Single-Junction Perovskite Solar Cells and the Role of Mobile Ions, *Sol. RRL*, 2021, **5**(8), 2100219.

12 P. Kumari, V. Srivastava, R. Khenata, S. A. Dar and S. H. Naqib, A first-principles prediction of thermophysical and thermoelectric performances of $SrCeO_3$ perovskite, *Int. J. Energy Res.*, 2022, **46**(3), 2934–2946, DOI: **10.1002/er.7354**. Available from: .

13 R. Yadav, A. Srivastava, R. Sharma, J. A. Abraham, S. A. Dar and A. K. Mishra, *et al.*, The study of optical and thermoelectric behaviour of thalium based flouroperovskite ($TlSiF_3$) for photovoltaic and renewable energy applications by DFT, *J. Solid State Chem.*, 2022, **313**, 123266, DOI: **10.1016/S0022459622003917**.

14 S. D. Stranks, G. E. Eperon, G. Grancini, C. Menelaou, M. J. P. Alcocer and T. Leijtens, *et al.*, Electron-hole diffusion lengths exceeding 1 micrometer in an organometal trihalide perovskite absorber, *Science*, 2013, **342**(6156), 341–344.

15 Y. Yuan, J. Chae, Y. Shao, Q. Wang, Z. Xiao and A. Centrone, *et al.*, Photovoltaic Switching Mechanism in Lateral Structure Hybrid Perovskite Solar Cells, *Adv. Energy Mater.*, 2015, **5**(15), DOI: **10.1002/aenm.201500615**.

16 D. Popovici, M. Okuyama and J. Akedo, Barium Titanate-Based Materials – a Window of Application Opportunities, *Ferroelectrics – Material Aspects*, InTech, 2011.

17 R. E. Newnham, *Structure–Property Relationships in Perovskite Electroceramics*, 2013, pp. 91–8.

18 M. Acosta, N. Novak, V. Rojas, S. Patel, R. Vaish and J. Koruza, *et al.*, $BaTiO_3$-based piezoelectrics: Fundamentals, current status, and perspectives, *Appl. Phys. Rev.*, 2017, **4**(4), DOI: **10.1063/1.4990046**.

19 V. Mishra, A. Sagdeo, V. Kumar, M. K. Warshi, H. M. Rai and S. K. Saxena, *et al.*, Electronic and optical properties of $BaTiO_3$ across tetragonal to cubic phase transition: An experimental and theoretical investigation, *J. Appl. Phys.*, 2017, **122**(6), DOI: **10.1063/1.4997939**.

20 J. Chen, H. Deng, D. Zheng, Y. Pan, S. Si and Y. Zhang, *et al.*, Band gap narrowing and electrical properties of $(1 − x)$-$BaTiO_{3−x}SrFe_{0.5}Nb_{0.5}O_3$ lead-free ceramics, *J. Mater. Sci.: Mater. Electron.*, 2021, **32**(8), 10151–10159.

21 J. M. V. Cunha, M. A. Barreiros, M. A. Curado, T. S. Lopes, K. Oliveira and A. J. N. Oliveira, *et al.*, Perovskite Metal–Oxide–Semiconductor Structures for Interface Characterization, *Adv. Mater. Interfaces*, 2021, **8**(20), 2101004.

22 J. Xu, D. P. Durisin and G. W. Auner, Optical properties of pulsed-laser deposited $BaTiO_3$ thin films, In *Photon Processing in Microelectronics and Photonics IV*, ed. J. Fieret, P. R. Herman, T. Okada, C. B. Arnold, F. G. Bachmann, W. Hoving, *et al.*, 2005, p. 305.

23 S. H. Wemple, Polarization fluctuations and the optical-absorption edge in $BaTiO_3$. *Phys. Rev. B.* 1970;2(7):2679–2689.

24 S. S. A. Gillani, R. Ahmad, M. Rizwan, M. Rafique, G. Ullah and C. B. Cao, *et al.*, Effect of magnesium doping on band gap and optical properties of $SrZrO_3$ perovskite: A first-principles study, *Optik*, 2019, **191**, 132–138.

25 M. I. Kholil, M. T. H. Bhuiyan, M. A. Rahman, M. S. Ali and M. Aftabuzzaman, Effects of Fe doping on the visible light absorption and bandgap tuning of lead-free ($CsSnCl_3$) and lead halide ($CsPbCl_3$) perovskites for optoelectronic applications, *AIP Adv.*, 2021, **11**(3), DOI: **10.1063/5.0042847**.

26 S. Das Adhikari, S. K. Dutta, A. Dutta, A. K. Guria and N. Pradhan, Chemically Tailoring the Dopant Emission in

Manganese-Doped CsPbCl$_3$ Perovskite Nanocrystals, *Angew. Chem., Int. Ed.*, 2017, **129**(30), 8872–8876, DOI: **10.1002/ange.201703863**.

27 N. Tanwar, S. Upadhyay, R. Priya, S. Pundir, P. Sharma and O. P. Pandey, Eu-doped BaTiO$_3$ perovskite as an efficient electrocatalyst for oxygen evolution reaction, *J. Solid State Chem.*, 2023, **317**, 123674, DOI: **10.1016/S002245962200799X**.

28 X. Luo, Y. Li, K. Liu and J. Zhang, Electron transport enhancement of perovskite solar cell due to spontaneous polarization of Li$^+$-doped BaTiO$_3$, *Solid State Sci.*, 2020, **108**, 106387, DOI: **10.1016/S1293255820312590**.

29 Z. Yao, H. Liu, Y. Liu, Z. Wu, Z. Shen and Y. Liu, *et al.*, Structure and dielectric behavior of Nd-doped BaTiO$_3$ perovskites, *Mater. Chem. Phys.*, 2008, **109**(2–3), 475–481, DOI: **10.1016/S0254058407007626**.

30 B. Mouhib, S. Dahbi, A. Douayar, N. Tahiri, O. El Bounagui and H. Ez-Zahraouy, Theoretical investigations of electronic structure and optical properties of S, Se or Te doped perovskite ATiO$_3$ (A = Ca, Ba, and Sr) materials for eco-friendly solar cells, *Micro and Nanostructures*, 2022, **163**, 107124, DOI: **10.1016/S0749603621003256**.

31 F. F. Li, D. R. Liu, G. M. Gao, B. Xue and Y. S. Jiang, Improved visible-light photocatalytic activity of NaTaO$_3$ with perovskite-like structure *via* sulfur anion doping, *Appl. Catal., B*, 2015, **166–167**, 104–111, DOI: **10.1016/S0926337314006699**.

32 T. Jia, Y. Hao and H. Hao, Sulfur-doping effects on oxygen vacancy formation in LaBO$_3$ (B = Fe, Co, and Ni) perovskites, *Phys. Chem. Chem. Phys.*, 2024, **27**(3), 1585–1592, DOI: **10.1039/D4CP03834G**.

33 J. Ran, T. Wang, J. Zhang, Y. Liu, C. Xu and S. Xi, *et al.*, Modulation of Electronics of Oxide Perovskites by Sulfur Doping for Electrocatalysis in Rechargeable Zn–Air Batteries, *Chem. Mater.*, 2020, **32**(8), 3439–3446, DOI: **10.1021/acs.chemmater.9b05148**.

34 Z. Ech-charqy, A. El Badraoui, A. Elkhou, M. Ziati and H. Ez-Zahraouy, Effect of sulfur doping on the electronic structures, optical and photocatalytic properties of KTaO$_3$ perovskites: DFT calculations, *Chem. Phys.*, 2025, **596**, 112759, DOI: **10.1016/S0301010425001600**.

35 H. Akter, M. A. Ali, M. M. Hossain, M. M. Uddin and S. H. Naqib, Oxysulfide perovskites: reduction of the electronic band gap of RbTaO$_3$ by sulfur substitution, *Phys. Scr.*, 2024, **99**(4), 045950, DOI: **10.1088/1402-4896/ad31f3**.

36 H. Akter, M. M. Hossain, M. M. Uddin, S. H. Naqib and M. A. Ali, Effects of S substitution on the structural, optoelectronic, and thermomechanical properties of KTaO$_3$ through density functional theory, *J. Phys. Chem. Solids*, 2024, **190**, 112021, DOI: **10.1016/S0022369724001562**.

37 U. Ahmed, H. Akter, A. Hossain, M. M. Hossian, M. M. Uddin and S. H. Naqib, *et al.*, Anion (S) substitution as a pathway for tuning the physical properties of CsTaO$_3$, *New J. Chem.*, 2025, **49**(18), 7682–7699.

38 J. W. Bennett, I. Grinberg and A. M. Rappe, Effect of substituting of S for O: The sulfide perovskite BaZrS$_3$ investigated with density functional theory, *Phys. Rev. B:*
Condens. Matter Mater. Phys., 2009, **79**(23), 235115, DOI: **10.1103/PhysRevB.79.235115**.

39 C. Zhang, Y. Jia, Y. Jing, Y. Yao, J. Ma and J. Sun, Effect of non-metal elements (B, C, N, F, P, S) mono-doping as anions on electronic structure of SrTiO$_3$, *Comput. Mater. Sci.*, 2013, **79**, 69–74, DOI: **10.1016/S0927025613003236**.

40 B. Wang, P. D. Kanhere, Z. Chen, J. Nisar, B. Pathak and R. Ahuja, Anion-doped NaTaO$_3$ for visible light photocatalysis, *J. Phys. Chem. C*, 2013, **117**(44), 22518–22524.

41 S. Dahbi, N. Tahiri, O. El Bounagui and H. Ez-Zahraouy, The new eco-friendly lead-free zirconate perovskites doped with chalcogens for solar cells: Ab initio calculations, *Opt. Mater.*, 2020, **109**, 110442.

42 G. Kresse and J. Furthmüller, Efficiency of ab-initio total energy calculations for metals and semiconductors using a plane-wave basis set, *Comput. Mater. Sci.*, 1996, **6**(1), 15–50.

43 J. P. Perdew, K. Burke and M. Ernzerhof, Generalized gradient approximation made simple, *Phys. Rev. Lett.*, 1996, **77**(18), 3865–3868.

44 J. Yang, L. Z. Tan and A. M. Rappe, Hybrid functional pseudopotentials, *Phys. Rev. B*, 2018, **97**(8), 085130.

45 H. Ehrenreich and M. H. Cohen, Self-consistent field approach to the many-electron problem, *Phys. Rev.*, 1959, **115**(4), 786–790.

46 V. Wang, N. Xu, J. C. Liu, G. Tang and W. T. Geng, VASPKIT: A user-friendly interface facilitating high-throughput computing and analysis using VASP code, *Comput. Phys. Commun.*, 2021, **267**, 108033.

47 A. Togo, L. Chaput, T. Tadano and I. Tanaka, Implementation strategies in phonopy and phono3py, *J. Phys.: Condens. Matter*, 2023, **35**(35), 353001.

48 S. J. Clark, M. D. Segall, C. J. Pickard, P. J. Hasnip, M. I. J. Probert and K. Refson, *et al.*, First principles methods using CASTEP, *Z. Kristallogr. Cryst. Mater.*, 2005, **220**(5–6), 567–570, DOI: **10.1524/zkri.220.5.567.65075/html**.

49 C. Srilakshmi, R. Saraf, V. Prashanth, G. M. Rao and C. Shivakumara, Structure and Catalytic Activity of Cr-Doped BaTiO$_3$ Nanocatalysts Synthesized by Conventional Oxalate and Microwave Assisted Hydrothermal Methods, *Inorg. Chem.*, 2016, **55**(10), 4795–4805, DOI: **10.1021/acs.inorgchem.6b00240**.

50 N. Inoue, T. Okamatsu, A. Ando, H. Takagi, T. Hashimoto and C. Moriyoshi, *et al.*, Structural Characteristics of (Ba$_{0.94}$Gd$_{0.06}$)(Ti$_{0.97}$Mg$_{0.03}$)O$_3$ in Cubic Structure Determined by High-Energy Synchrotron-Radiation Powder Diffraction, *Jpn. J. Appl. Phys.*, 2009, **48**(9), 09KF03, DOI: **10.1143/JJAP.48.09KF03**.

51 R. D. Shannon, Revised effective ionic radii and systematic studies of interatomic distances in halides and chalcogenides, *Acta Crystallogr., Sect. A:Found. Crystallogr.*, 1976, **32**(5), 751–767.

52 A. E. Fedorovskiy, N. A. Drigo and M. K. Nazeeruddin, The Role of Goldschmidt's Tolerance Factor in the Formation of A$_2$BX$_6$ Double Halide Perovskites and its Optimal Range. Small, *Methods*, 2020, **4**(5), 1900426.

53 C. Li, X. Lu, W. Ding, L. Feng, Y. Gao and Z. Guo, Formability of ABX$_3$ (X = F, Cl, Br, I) halide perovskites, *Acta Crystallogr., Sect. B: Struct. Sci.*, 2008, **64**(6), 702–707.

54 M. W. Qureshi, X. Ma, G. Tang and R. Paudel, Ab initio predictions of structure and physical properties of the Zr$_2$GaC and Hf$_2$GaC MAX phases under pressure, *Sci. Rep.*, 2021, **11**(1), 3260.

55 S. Nakamura, Y. Tsuji and K. Yoshizawa, Molecular Dynamics Study on the Thermal Aspects of the Effect of Water Molecules at the Adhesive Interface on an Adhesive Structure, *Langmuir*, 2021, **37**(50), 14724–14732, DOI: **10.1021/acs.langmuir.1c02653**.

56 F. Rahman, M. M. Ali, M. A. Ali, M. M. Uddin, S. H. Naqib and M. M. Hossain, DFT approach into the physical properties of MTe$_3$ (M = Hf, Zr) superconductors: A comprehensive study, *AIP Adv.*, 2023, **13**(8), DOI: **10.1063/5.0160012**.

57 M. A. Ali, M. Anwar Hossain, M. A. Rayhan, M. M. Hossain, M. M. Uddin and M. Roknuzzaman, *et al.*, First-principles study of elastic, electronic, optical and thermoelectric properties of newly synthesized K$_2$Cu$_2$GeS$_4$ chalcogenide, *J. Alloys Compd.*, 2019, **781**, 37–46.

58 J. Feng and B. Xiao, Effective masses and electronic and optical properties of nontoxic MASnX$_3$ (X = Cl, Br, and I) perovskite structures as solar cell absorber: A theoretical study using HSE06, *J. Phys. Chem. C*, 2014, **118**(34), 19655–19660.

59 J. Gao, W. Zeng, B. Tang, M. Zhong and Q. J. Liu, Optical, electronic, and mechanical properties of p-type conductive oxide BaBiO$_3$: A density functional theory study, *Chem. Phys. Lett.*, 2020, **761**, 138054.

60 S. Park, B. Lee, S. H. Jeon and S. Han, Hybrid functional study on structural and electronic properties of oxides, *Curr. Appl. Phys.*, 2011, **11**(3 Suppl.), S337–S340.

61 R. Schira and C. Latouche, DFT and hybrid-DFT calculations on the electronic properties of vanadate materials: Theory meets experiments, *New J. Chem.*, 2020, **44**(27), 11602–11607.

62 W. Shockley and H. J. Queisser, Detailed balance limit of efficiency of p-n junction solar cells, *J. Appl. Phys.*, 1961, **32**(3), 510–519.

63 B. Ehrler, E. Alarcón-Lladó, S. W. Tabernig, T. Veeken, E. C. Garnett and A. Polman, Photovoltaics reaching for the shockley-queisser limit, *ACS Energy Lett.*, 2020, **5**(9), 3029–3033.

64 Y. Xu, T. Gong and J. N. Munday, The generalized Shockley-Queisser limit for nanostructured solar cells, *Sci. Rep.*, 2015, **5**(1), 13536.

65 S. Azam, S. Goumri-Said, S. A. Khan and M. B. Kanoun, Electronic, optical and thermoelectric properties of new metal-rich homological selenides with palladium–indium: Density functional theory and Boltzmann transport model, *J. Phys. Chem. Solids*, 2020, **138**, 109229.

66 F. Chiker, B. Abbar, B. Bouhafs and P. Ruterana, Interband transitions of wide-band-gap ternary pnictide BeCN$_2$ in the chalcopyrite structure, *Phys. Status Solidi B*, 2004, **241**(2), 305–316.

67 M. Hilal, B. Rashid, S. H. Khan and A. Khan, Investigation of electro-optical properties of InSb under the influence of spin-orbit interaction at room temperature, *Mater. Chem. Phys.*, 2016, **184**, 41–48.

68 C. Ambrosch-Draxl and J. O. Sofo, Linear optical properties of solids within the full-potential linearized augmented planewave method, *Comput. Phys. Commun.*, 2006, **175**(1), 1–14.

69 V. K. Rashenov, M. G. Foigel and R. A. Alarashi, Dielectric Function of a Model Semiconductor, *Phys. Status Solidi*, 1972, **54**(1), 355–368.

70 D. R. Penn, Wave-number-dependent dielectric function of semiconductors, *Phys. Rev.*, 1962, **128**(5), 2093–2097.

71 M. A. Rahman, R. Khatun, R. Ferdous, D. Chandra Roy, M. Z. Hasan and A. Irfan, *et al.*, First-principles calculations to investigate structural, elastic, electronic, optical and thermal properties of La-based ternary intermetallic superconductors LaM$_2$Si$_2$ (M = Co, Cu, Rh, Pd, Ag, Ir, Pt, Au), *J. Mater. Res. Technol.*, 2023, **26**, 3840–3862.

72 P. R. Varadwaj and H. M. Marques, Physical and optoelectronic features of lead-free A$_2$AgRhBr$_6$ (A = Cs, Rb, K, Na, Li) with halide double perovskite composition, *J. Mater. Chem. C*, 2020, **8**(37), 12968–12983.

73 A. Bafekry, M. Shahrokhi, A. Shafique, H. R. Jappor, M. M. Fadlallah and C. Stampfl, *et al.*, Semiconducting chalcogenide alloys based on the (Ge, Sn, Pb) (S, Se, Te) formula with outstanding properties: A first-principles calculation study, *ACS Omega*, 2021, **6**(14), 9433–9441.

74 H. H. Hegazy, G. M. Mustafa, A. Nawaz, N. A. Noor, A. Dahshan and I. Boukhris, Tuning of direct bandgap of Rb$_2$ScTlX$_6$(X = Cl, Br, I) double perovskites through halide ion substitution for solar cell devices, *J. Mater. Res. Technol.*, 2022, **19**, 1271–1281.

75 A. El Amrani, A. Bekhtari, A. El Kechai, H. Menari, L. Mahiou and M. Maoudj, *et al.*, Determination of the suitable refractive index of solar cells silicon nitride, *Superlattices Microstruct.*, 2014, **73**, 224–231.

76 M. H. Mia, U. Ahmed, S. K. Saha and M. A. Ali, Unveiling mechanical, electronic, and optical properties of newly synthesized Mo$_2$VAlC$_2$ and Mo$_2$V2AlC$_3$ o-MAX phases via first-principles calculations, *J. Mater. Res. Technol.*, 2025, **36**, 2468–2484.

77 R. Hill, The elastic behaviour of a crystalline aggregate, *Proc. Phys. Soc., London, Sect. A*, 1952, **65**(5), 349–354.

78 F. Mouhat and F. X. Coudert, Necessary and sufficient elastic stability conditions in various crystal systems, *Phys. Rev. B: Condens. Matter Mater. Phys.*, 2014, **90**(22), 224104.

79 A. F. Young, C. Sanloup, E. Gregoryanz, S. Scandolo, R. J. Hemley and H. K. Mao, Synthesis of novel transition metal nitrides IrN$_2$ and OsN$_2$, *Phys. Rev. Lett.*, 2006, **96**(15), 155501, DOI: **10.1103/PhysRevLett.96.155501**.

80 M. Hebbache, Shear modulus and hardness of crystals: Density functional calculations, *Solid State Commun.*, 2000, **113**(8), 427–432, DOI: **10.1016/S0038109899005141**.

81 I. R. Storch, R. De Alba, V. P. Adiga, T. S. Abhilash, R. A. Barton and H. G. Craighead, *et al.*, Young's modulus

and thermal expansion of tensioned graphene membranes, *Phys. Rev. B*, 2018, **98**(8), 085408, DOI: **10.1103/PhysRevB.98.085408**.

82 Y. Tian, B. Xu and Z. Zhao, Microscopic theory of hardness and design of novel superhard crystals, *Int. J. Refract. Met. Hard Mater.*, 2012, **33**, 93–106.

83 X. Q. Chen, H. Niu, D. Li and Y. Li, Modeling hardness of polycrystalline materials and bulk metallic glasses, *Intermetallics*, 2011, **19**(9), 1275–1281.

84 M. A. Hossain, M. S. Ali and A. K. M. A. Islam, Rare earth rhodium borides RRh_3B (R = Y, Zr, and Nb): mechanical, thermal and optical properties, *Eur. Phys. J. B*, 2012, **85**(12), 396.

85 C. Toher, J. J. Plata, O. Levy, M. De Jong, M. Asta and M. B. Nardelli, *et al.*, High-throughput computational screening of thermal conductivity, Debye temperature, and Grüneisen parameter using a quasiharmonic Debye model, *Phys. Rev. B: Condens. Matter Mater. Phys.*, 2014, **90**(17), 174107.

86 F. W. De Wette and A. D. Kulkarni, Phonon dispersion, phonon specific heat, and Debye temperature of high-temperature superconductors, *Phys. Rev. B: Condens. Matter Mater. Phys.*, 1992, **46**(22), 14922–14925.

87 Z. Ali, I. Khan, I. Ahmad, M. S. Khan and S. J. Asadabadi, Theoretical studies of the paramagnetic perovskites $MTaO_3$ (M = Ca, Sr and Ba), *Mater. Chem. Phys.*, 2015, **162**, 308–315.

88 M. E. Fine, L. D. Brown and H. L. Marcus, Elastic constants versus melting temperature in metals, *Scr. Metall.*, 1984, **18**(9), 951–956.

89 Z. Tong, Y. Zhang, A. Pecchia, C. Y. Yam, L. Zhou and T. Dumitrică, *et al.*, Predicting the Lattice Thermal Conductivity in Nitride Perovskite $LaWN_3$ from ab initio Lattice Dynamics, *Adv. Sci.*, 2023, **10**(9), 2205934.

90 O. Delaire, A. F. May, M. A. McGuire, W. D. Porter, M. S. Lucas and M. B. Stone, *et al.*, Phonon density of states and heat capacity of $La_{3-x}Te_4$, *Phys. Rev. B: Condens. Matter Mater. Phys.*, 2009, **80**(18), 184302.